ABSTRACT

Title of thesis: INVESTIGATION AND CHARACTERIZATION OF A CYCLOIDAL ROTOR FOR APPLICATION TO A MICRO-AIR VEHICLE

Eric Parsons, Master of Science, 2005

Directed by: Professor/Advisor, Inderjit Chopra
Department of Aerospace Engineering

In recent years, interest has been growing in a new class of very small flight vehicles called micro air vehicles (MAVs). The use of cycloidal propulsion for such a vehicle has some advantages over other configurations that make it an attractive alternative to fixed-wing and rotary-wing vehicles. In a cycloidal blade system, a series of blades rotate around an axis of rotation oriented parallel to both the blades and the horizon. As the blades rotate about the axis, their pitch angle is varied periodically.

This paper investigates a small scale cycloidal rotor to determine its viability for use on a micro air vehicle. An analytical model, using a combination of wind turbine theory and an indicial solution for the aerodynamic response was developed in an attempt to predict rotor performance. A small experimental rotor was constructed and tested to determine the effects of blade number, blade pitch angle, and rotational speed on thrust output, power requirements, and efficiency. While a six-bladed configuration demonstrated more thrust production than a three-bladed one,

results showed lower efficiency than that predicted and may suffer from blade-wake interference. High blade pitch angles of 30° to 40° are necessary to meet thrust requirements for an MAV.

Experimental results are compared with predictions as well as to results from a conventional rotor to ascertain the effectiveness of the cycloidal configuration. A maximum figure of merit of approximately 0.55 is achieved during testing, comparable with the conventional rotor. However, figure of merit for the cycloidal rotor declines as rotational speed increases, severely limiting its usefulness if high efficiency is necessary. An investigation of the flow field around the rotor is conducted to achieve an acceptable quantitative picture of the rotor downwash. Results demonstrate that outflow is directed approximately 15° from the vertical. Although it appears that flow may expand upon exiting the rotor, results are inconclusive at this time.

An MAV utilizing cycloidal propulsion is modeled in CATIA to determine its viability. The cyclo-MAV utilizes two cycloidal rotors, providing thrust, propulsion, and control. Complete vehicle weight is 240 grams. Based on the experimental results, it is feasible to construct a micro air vehicle using cycloidal propulsion.

INVESTIGATION AND CHARACTERIZATION OF A CYCLOIDAL ROTOR FOR APPLICATION TO A MICRO AIR VEHICLE

by

Eric Parsons

Thesis submitted to the Faculty of the Graduate School of the
University of Maryland, College Park in partial fulfillment
of the requirements for the degree of
Master of Science
2005

Advisory Commmittee:

Professor Inderjit Chopra, Chair/Advisor
Professor James Baeder
Professor J. Gordon Leishman
Dr. Jayant Sirohi, Research Scientist/Advisor

ACKNOWLEDGMENTS

I would like to thank my advisor, Dr. Inderjit Chopra, for providing me with the opportunity to work under his direction over the past two years. His guidance has been invaluable, and it has been a pleasure to study under his tutelage.

I would also like to thank my co-advisor, Dr. Jayant Sirohi. I could not have accomplished what I have without his encouragement and advice, and I am greatly in his debt.

I would also like to thank the other members of my examining committee, Dr. James Baeder and Dr. J. Gordon Leishman, for agreeing to serve on my examining committee and for sparing their invaluable time reviewing my work.

My associates at the Rotorcraft Center have greatly enriched my graduate life and deserve special mention. My colleagues in the the lab have taught me more than I would have thought possible, and I have become a better person because of them. I would thank all of you, Shaju John, Jinsong Bao, Dr. Nagaraj, Ron Couch, Jaye Falls, Felipe Bohorquez, Benjamin Hein, Daniel Everson, Anne Brindejonc, and Beerinder Singh.

My deepest thanks to my family - my mother and father who have always supported me and provided guidance and encouragement, and my sisters, for whose support I am grateful.

I would like to acknowledge financial support from the Army Research Office

(ARO) for all the projects discussed herein.

It is impossible to mention all those who have helped me through this along my journey at the University of Maryland, and I apologize to those I may have inadvertently left out. I owe my gratitude to all the people who have made my time here possible. It is because of them that my graduate experience has been one that I will cherish forever.

TABLE OF CONTENTS

LIST OF TABLES

LIST OF FIGURES

Nomenclature

a = pivot point of the airfoil measured from mid-chord, aft positive

AR = aspect ratio of blade

b = semi-chord of airfoil

c = chord of airfoil

C_D = drag coefficient of the blade

C_{D_o} = parasitic drag coefficient

C_{l_α} = 2-D lift curve slope of airfoil

C_{L_α} = 3-D lift curve slope of airfoil

C_L = lift coefficient of blade

C_{F_x} = thrust coefficient of the rotor (x-force only)

C_{F_z} = thrust coefficient of the rotor (z-force only)

C_P = power coefficient of the rotor

C_T = thrust coefficient of the rotor

dA = area of actuator disk used in momentum analysis

dS = unit normal area vector of control volume used in momentum analysis

DL = disk loading

e = Oswald span efficiency factor

F_{norm} = force produced by a blade normal to its circular path around the rotor azimuth

F_{tan} = force produced by a blade tangent to its circular path around the rotor azimuth

F_{res} = resultant force of F_x and F_z

F_x = force produced by the rotor in the x direction

F_z = force produced by the rotor in the z direction

FM = figure of merit

k = reduced frequency

L^c = circulatory lift of the airfoil

$\dot{m}$ = mass flow rate

M_a = moment about the pitching axis of the airfoil

P = power required by the rotor

PL = power loading

Q = rotor torque

R = rotor diameter

Re = Reynolds number

s = reduced time

s = blade spacing

S = surface area of control volume used in momentum analysis

T = torque produced by the rotor

U_P = local velocity on any blade element normal to the circular path swept by the blade as it moves around the rotor azimuth

U_R = resultant velocity of U_P and U_T

U_T = local velocity on any blade element tangential to the circular path swept by the blade as it moves around the rotor azimuth

v_d = induced velocity, downstream half of rotor

v_u = induced velocity, upstream half of rotor

V_t = tip speed of blades, R*Ω

V_∞ = far upstream velocity of upstream half of rotor

w = far wake induced velocity of upstream half of rotor and far upstream velocity of downstream half of rotor

w_∞ = far wake induced velocity of downstream half of rotor

$\dot{W}$ = instantaneous rate of work done to maintain an oscillating airfoil

α = angle of attack

α_n = angular acceleration of blade about pivot point

δ = Dirac function

ϕ = phase angle of eccentricity of the rotor measured counterclockwise from the negative z axis

ϕ = induced angle of attack

ϕ_s = Wagner's function

λ_h = hover inflow ratio

θ = blade pitch angle measured with respect to the tangent of the blade's circular path around the rotor azimuth

θ_{max} = amplitude of the blade pitch oscillation

$\dot{\theta}$ = angular velocity of blade about its pivot point (quarter-chord)

$\ddot{\theta}$ = angular acceleration of blade about its pivot point (quarter-chord)

ω = angular velocity of blade about pivot point

Ω = rotational speed of cycloidal rotor

Ψ = blade position around the azimuth of the rotor measured counterclockwise from the negative z axis

Chapter 1

Introduction

1.1 Problem Statement

In recent years, interest has been growing in a new class of very small flight vehicles called micro air vehicles (MAVs). This interest has developed, in part, by the changing needs of the military as the battlegrounds of the future move to restricted, highly populated urban environments where conventional aircraft lose much of their utility.

1.1.1 MAV Definition

The Defense Advanced Research Projects Agency (DARPA), which has taken a significant interest and a leading role in developing the technology necessary to make micro air vehicles a reality, has defined the class to a size less than 15 cm (approx. six inches) in length, width, or height [1]. This definition places MAVs an order of magnitude smaller in size than current flying vehicles, and comparable to large insect or small birds. Fig. 1.1 illustrates the scales of various types of flying vehicles [1].

DARPA has put forth significant resources towards the maturation of MAV technology for military use, with its ultimate goal being the development of backpackable systems capable of providing local reconnaissance, targeting, and commu-

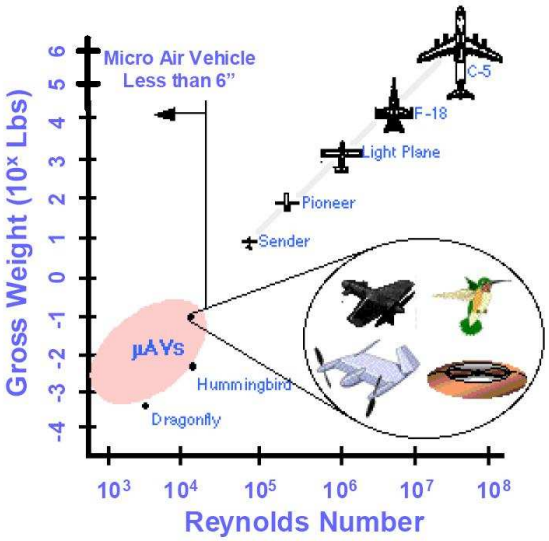

Figure 1.1: MAV Flight Regime

nications to platoon-level groups, "reducing latency inherent in current reconnaissance" methods [1]. This would provide an unprecedented increase in situational awareness and on-demand information to soldiers, increasing overall effectiveness. DARPA's initial program objectives are to develop the technology and components necessary to achieve efficient flight at small scales, with specific targets of a desired endurance limit of 20 to 60 minutes, a range of ten kilometers, weight of 100 grams, and a payload of 20 grams.

1.1.2 MAV Missions

The small size of MAVs makes them ideally suited for a wide variety of missions, both military and civilian. The most obvious use, from a military perspective, is for reconnaissance. MAVs provide the ideal platform for over-the-hill surveillance, providing real-time local information to troops without exposing them to

danger. With the proper payloads, MAVs could be outfitted for tasks ranging from biological-chemical agent detection, real-time day/night imaging, damage assessment, and battlefield communications. Eventually, they may even be outfitted with or used as weapons, such as remote precision mines [2].

MAVs promise to be extremely useful in the urban warfare environment, which has emerged as the main arena of warfare, at least for the next few decades. The complex topology, high civilian concentration, and restricted operating areas make it impossible to make use of current air vehicles. Small, maneuverable vehicles, such as MAVs, offer the possibility of enormously reducing the risks to military personnel who must operate in such conditions by allowing them to perform their duties without exposing themselves to danger.

Although DARPA's interest in them is primarily for use by the military, MAVs can perform many functions other than those envisioned by the military. These vary from functions such as border surveillance, fire-and-rescue, or counter-drug operations, to more mundane tasks like traffic monitoring, seismic detection, and forestry and wildlife surveys. In the commercial sector, they could perform duties ranging from communications relays or power-line inspection to real-estate aerial photography and agricultural monitoring.

1.1.3 MAV Considerations

A number of enabling technologies must first be developed and refined for micro air vehicles to be viable. Areas currently under investigation include low

Reynolds number aerodynamics, flight control, navigation, propulsion, communications, and vehicle design.

Aerodynamics

DARPA's size limits on MAVs derive from both physical and technological considerations. Referring to Fig. 1.1, the Reynolds numbers at which MAVs typically operate, ranging from 10,000 to 100,000, demonstrate a fundamental shift in the physics of the flight environment. For instance, traditional full-scale quasi-steady aerodynamics cannot explain how bees produce enough lift to fly. Likewise, the range of wasps and the agility of hummingbirds cannot be explained by conventional quasi-steady aerodynamics. However, as nature has shown that each of these cases is indeed possible, there must be a lack of physical understanding of flight mechanics at these scales.

Furthermore, from investigation of both insects and small-scale vehicles, a higher ratio of wing area-to-vehicle weight is required to achieve flight. This necessitates low aspect ratio wings, which introduces three-dimensional aerodynamics into an already complex problem. Relative to full scale vehicles, the high viscosity, low Reynolds number flow experienced by MAVs creates a high section drag and thick boundary layers, leading to thick vortex sheets in the wake.

For this reason, experimental data is critical in predicting performance for MAV-scale vehicles. For instance, conventional airfoils experience very poor performance at low Reynolds numbers. Bohorquez et al. [3] and Hein et al. [4] have

expended considerable effort in determining optimal airfoil design for MAV rotors by investigating the effects of solidity, twist, taper, camber, and tip shape. Their efforts have led to an increase in figure of merit at MAV scales from 0.38 to 0.68. Extensive research in airfoils for fixed wing vehicles has also been conducted.

Flight Control

Flight control is another area where MAVs encounter significant differences from larger vehicles. The proportionally large forces and moments that arise in the low Reynolds number, partially laminar flow which dominates the flight regime of MAVs are very difficult to predict using current methodologies [1]. Moreover, unsteady effects, both from the flight mechanics and from environmental concerns, such as wind gusts, cause much more pronounced effects on MAVs than on larger vehicles. The very low wing loadings and inertial forces experienced by such small vehicles also present problems, as these are typically stabilizing forces on a vehicle.

Compounding the problem, MAVs must be user-friendly to be of practical use for military operations, as it is desirable that a large cross-section of personnel can operate the system without extensive training. Moreover, in critical situations a soldier may be faced with a multitude of tasks and greatly increased stress levels; anything that might detract from their ability to concentrate on the mission is a liability. Therefore, to be a useful asset for the military, a MAV must be, to some extent, intuitive, with the learning curve kept as short as possible.

For these reasons, flight control holds some of the greatest challenges for in-

tegrating MAVs into current systems, and so many research initiatives are investigating this field. At the University of Maryland, Everson et al. [5] are currently conducting experiments for the determination of stability derivatives of micro air vehicles. These may then be used to optimize its flying qualities. This is not only useful in creating a more stable vehicle but will be necessary for the development of control algorithms for autonomous or semi-autonomous MAVs in the future.

Navigation

Self-navigation is important for an MAV to navigate successfully in areas where the terrain is unknown, as well as in confined spaces, such as building interiors. Current navigation methods, such as GPS or inertial navigation, are either too heavy and power-intensive or await development of new technologies before they can be implemented on MAVs. In light of this, novel methods are being considered. Conroy et al. [6] is developing a navigation system based on optic flow, in many ways mimicking the ways in which many insects navigate. This method not only serves as a guidance system for the craft, but also as an automatic landing system. A concern, however, is that the MAV would still need to carry cameras to conduct reconnaissance missions. Srinivasan et al. [7] are investigating a lightweight, compact vision system that provides panoramic vision, panoramic optic flow, and panoramic stereo vision. This system has the capability to function for both navigation and surveillance.

Propulsion

Propulsion is another area of concern for MAVs, as no current technology is suitable for their use for long endurance. One of the limiting factors of MAVs currently in development is expanding their short endurance. Rotary-wing vehicles, especially, have very limited flight times because of their high power requirements relative to fixed-wing vehicles. Research in this area is divided with respect to the best solution to the problem. Batteries and motors are very efficient at converting stored energy into usable energy, but have a low energy density. On the other hand, gasoline has a very high energy density, but internal combustion engines are extremely inefficient at small scales. As the engine grows smaller, its surface-to-volume ratio increases, leading to greater heat loss and decreased efficiency. At this stage, current MAVs employ batteries, as they have the additional advantage of reduced acoustic signatures. However, research in both areas continues.

Communications

Scenarios envisioned for MAVs generally limit them to a range of about ten kilometers. Current wireless communications, however, cannot provide the range necessary over those distances. Both Bluetooth and WiFi, the current standards in wireless communication, are limited to shorter ranges. With the limited power on board an MAV, an omni-directional signal will be too weak to be useful. Directional ground antennas could be employed to track the vehicle, but this limits the MAV to line-of-sight use, severely decreasing its usefulness. Furthermore, a transmission

rate of 2–4 megabits/sec is required to send images necessary for reconnaissance missions, with video requiring a much higher bandwidth. Current systems cannot provide this utility. Note, much of the work being performed in this area by the consumer electronics industry may be applied to MAVs once it has matured.

Vehicle Design Considerations

Operation in confined spaces and highly populated urban areas require MAVs to be compact. For military use, it is desired that the entire system (MAV, sensors, receiver, control methods) be backpackable – capable of being transported by a single soldier. Under the same considerations, the system must be lightweight. This is necessary not only for the vehicle itself, where weight has deleterious effects on flying characteristics and power requirements, but for the control system as well, as it will displace other assets. These same reasons demand MAVs to be highly maneuverable. Flying indoors or between buildings requires an agile and responsive vehicle.

Considering the environments and conditions in which they will be employed, especially military applications, MAVs must be extremely robust. Ambient temperatures, wind, and moisture will vary with location, and all must be considered during design. If a launching system is necessary, as is currently envisioned for operation from submarines, the MAV and its components could be subjected to extreme forces and shock during the launch.

Military operations generally call for more stringent requirements on equip-

ment than civilian applications, and MAVs as such are no exception. Rapid deployment, real-time data acquisition, and low acoustic signature are all critical for any acceptable surveillance platform. All weather operations and collision avoidance are also highly desirable characteristics.

Current aircraft systems are composed of an outer shell (frame), into which the necessary components for flight are fit. However, the high surface-to-volume ratio of such small vehicles creates severe weight and volume limitations. The use of multi-functional systems, therefore, becomes necessary to achieve the desired objectives. AeroVironment's WASP, for example, includes a battery formed as part of the wing structure (Fig. 1.2), minimizing unnecessary weight [8]. Antennae or sensors could also be constructed as an integral component of the wing. MEMS (Micro-Electro-Mechanical Systems) is an enabling technology that will allow sensors, actuators, and control components to be combined onto a single chip through microfabrication techniques.

Finally, a successful MAV must be affordable. Any design that is prohibitively expensive will not be fielded in large numbers. Manufacturing methods and system components will need to be optimized to reduce development and acquisition costs.

1.2 MAV Configurations

A number of vehicle configurations are being considered for MAVs due to the wide variety of roles for which they will be used, and no single configuration is best suited for all such missions. Initial efforts have concentrated on familiar

Figure 1.2: AeroVironment WASP

areas, such as fixed- and rotary-wing aircraft. However, as the technology matures, unusual types of configurations that had hitherto been impractical will come into more frequent use as some, such as flapping wings, hold great promise.

1.2.1 Fixed Wing

The most mature designs thus far are small fixed wing vehicles, such as Lockheed Martin's Microstar [9], Fig. 1.3, or Aerovironment's Black Widow [8], Fig. 1.4. These vehicles have shown excellent range and endurance characteristics, while achieving low vehicle gross weight. Their primary drawbacks are their inability to hover and minimum flight speeds of around 30 miles per hour. These weaknesses effectively limit their usefulness for either surveillance or operation in confined spaces.

Figure 1.3: Lockheed Martin Microstar MAV

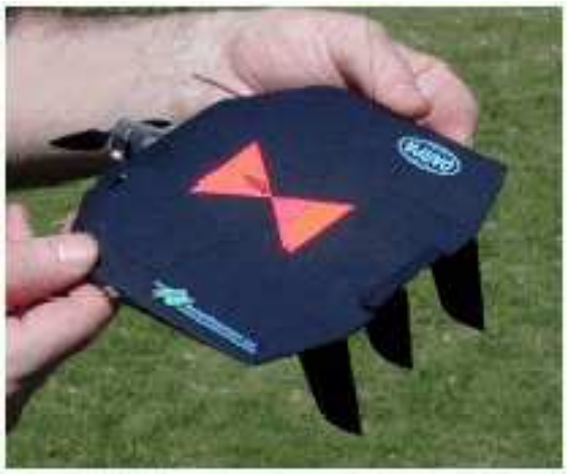

Figure 1.4: AeroVironment Black Widow

1.2.2 Rotary Wing

Rotary wing micro air vehicles have also been investigated. The Seiko FR1 [10] and MICOR [3], developed at the University of Maryland, demonstrate the utility of such designs, and it is highly probable that rotary-wing MAVs will be the most successful designs in the early stages. Their hover capability is their primary advantage over fixed wing designs, but it comes at a high cost. Rotary wing designs have low endurance, low payload, and limited flight speeds compared to fixed wing MAVs. Furthermore, power requirements are greater, and response time is very slow. Even with these deficiencies, however, rotary wing MAVs provide the best choice for a platform to perform in constrained areas.

Figure 1.5: Seiko FR1 Rotary Wing MAV

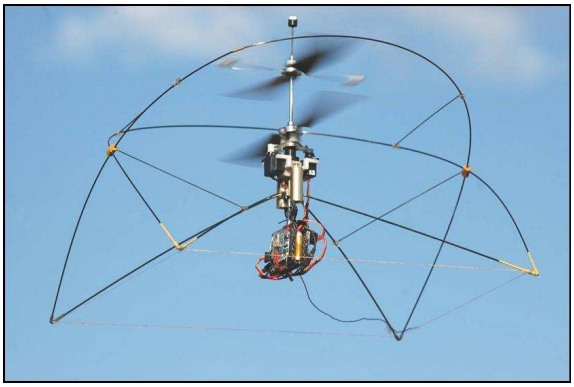

Figure 1.6: University of Maryland MICOR

1.2.3 Unconventional

Flapping Wing

The enormous challenges that must be faced in developing successful micro air vehicles has led many groups to conclude that unconventional configurations may provide the greatest opportunity for success. In this respect, flapping wing vehicles have received the most attention; AeroVironment's Microbat and UC Berkeley's Robofly, shown in Figs. 1.7 and 1.8, provide excellent examples of this configuration. The challenges facing a viable flapping wing MAV, however, are numerous. Insect wings, for example, undergo very large pitch changes and complex motions to take advantage of a variety of unusual flight mechanisms necessary at low Reynolds numbers. To take advantages of those same mechanisms, however, would require an MAV to undergo similar motions, requiring complex actuation mechanisms that, at this time, suffer from weight considerations. A limited understanding of wing aeroelasticity, seen in the large deformations of insect wings in flight, has also posed

problems. At the low Reynolds numbers at which flapping wing flight becomes beneficial, unsteady aerodynamics become very important. Mechanisms such as clap-fling and dynamic stall vortices provide the lift necessary to make small-scale flight possible, but are not fully understood at this time. At the University of Maryland, Singh et al. [11] have attempted to quantify some of these mechanisms, but the large inertial loads and viscous dominated vertical flows make experiments extremely difficult. For these reasons, while flapping wing flight has the potential to greatly increase the capabilities of MAVs, the difficulties in accomplishing it at this time are too numerous.

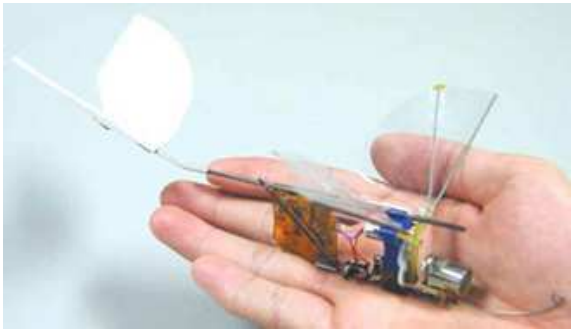

Figure 1.7: AeroVironment Microbat

Cycloidal Rotor

One configuration that has not received much attention, but has the potential to solve or alleviate many of the problems facing current micro air vehicle designs, is the cycloidal rotor. Illustrated in Fig. 1.9, the cycloidal blade system may be considered a horizontal rotary wing, with its blade span parallel to a horizontal axis of rotation. As the blades rotate around the azimuth, their pitch angle is

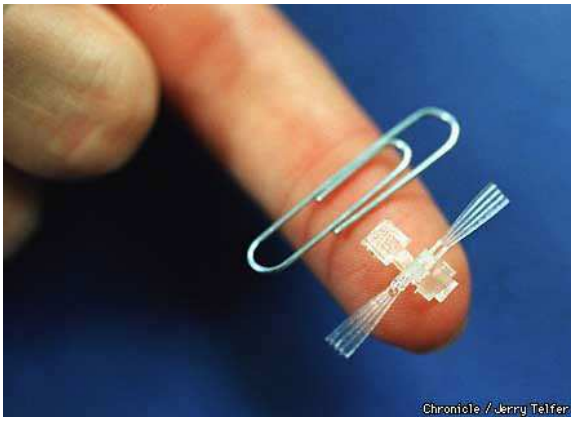

Figure 1.8: UC Berkeley Robofly

varied periodically, shown in Fig. 1.10. Each blade element operates at the same conditions – velocity, Reynolds number, angle of attack, centrifugal force – and thus can be set at its greatest efficiency. Some recent experiments have claimed cycloidal rotors to be at least twice as efficient as a conventional rotor [12]. Moreover, they have the ability to change the direction of thrust almost instantly. An MAV utilizing cycloidal rotors would have a hover capability similar to rotary wing vehicles, and a possible efficiency somewhere between rotary wing and fixed wing vehicles.

1.3 Previous Work/State of the Art

While the concept of cycloidal propulsion is quite old, it has remained obscure until recently. Nagler [13] constructed and tested a "paddlewheel" airplane in 1926, and measured very high lift from the design. However, he could not work out an economical solution for the high centrifugal loads acting on the blades, and discontinued the project.

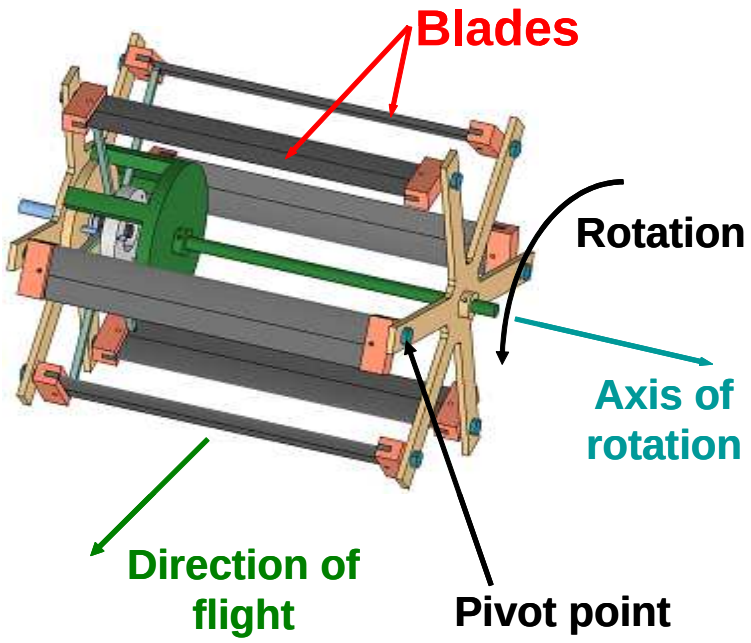

Figure 1.9: Cycloidal Rotor

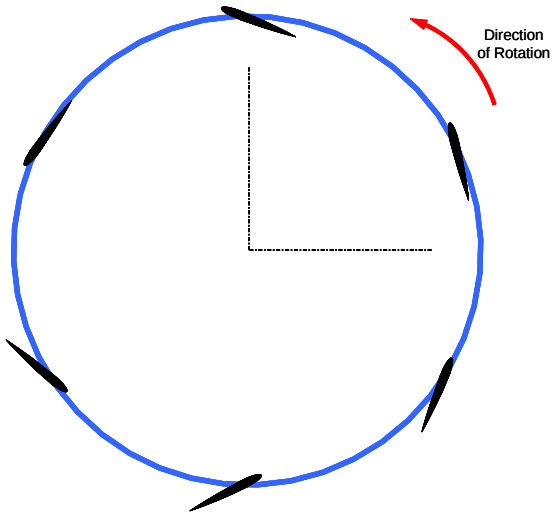

Figure 1.10: Cycloidal Rotor Cross-Section

Kirsten [14] investigated cycloidal propulsion at the University of Washington in the 1920s. He constructed a large cycloidal propeller and began investigating its use for air vehicles. However, funding dried up for the project, and when he received a grant from the Navy, he began looking into means of applying cycloidal propulsion to marine systems. Today, Kirsten's cycloidal propellers are used extensively by tug boats, providing them with the maneuverability necessary to operate in confined harbors.

In the 1930s, Wheatley [15] developed a simplified aerodynamic theory of a cyclogiro rotating wing and conducted wind tunnel tests on a large four-bladed prototype rotor with diameter and span of eight feet. Blades used a NACA 0012 airfoil profile and had a chord of 0.312 ft. He too, measured significant thrust levels, but achieved poor agreement between his theory and experiment [16].

More recently, McNabb [17] developed a computer model for a cycloidal propeller and compared the predictions with experimental results of thrust and power measured on a rotor constructed by Bosch Aerospace. The model consisted of a six-bladed propeller with a diameter and span of four feet. NACA 0012 airfoil sections were used for the blades, each with a chord of one foot. Maximum blade pitch angle was fixed at 25 degrees, and rotational speeds up to 650 RPM were tested. The model generated 138 lb of lift and required 28 hp at 600 RPM. McNabb's predictions were within five percent of the experimental results.

Bosch Aerospace, working in conjunction with Mississippi State University, has been developing cycloidal propulsion technology for use on lighter than air (LTA) vehicles [18], [19], [20]. Although a model rotor has been constructed, testing has

not been completed.

Kim et al. [12, 21] constructed and tested a cycloidal propeller with a radius of 0.4 meters and a span of 0.8 meters. The blades used a NACA 0012 airfoil, with chord of 0.15 meters. A mechanism was devised such that blade pitch angle could be varied; number of blades was also varied. Maximum thrust measured was 4.6 kgf at 500 RPM, a blade pitch angle of 30 degrees, and a phase angle of 10 degrees. A thrust-to-power ratio of 5.6 kgf/hp was achieved in this configuration. An analysis was also conducted using CD Adopco/Star-CD commercial CFD software to predict rotor characteristics. It was found that thrust was proportional to the square of rotational speed, and power to the cube of rotational speed, as expected [12].

At the University of Maryland, Belloli, Sirohi, and Chopra [22] constructed a prototype MAV-scale cycloidal rotor with diameter and span of six inches. Blades used an NACA 0010 profile and had a chord of one inch. Maximum blade pitch angle was 10 degrees. A quasi-steady analytical model was developed and preliminary tests were performed to measure thrust and power. The predictions did not match well with experiment; however, results of the experiment showed promise and warranted further research.

Although they generally possess fixed pitch blades, vertical axis windmills (VAWTs) experience a motion similar to cycloidal rotors, and a large body of work has been conducted in developing aerodynamic performance prediction methods for them [23], [24], [25]. While it comprises only a very small percentage of existing VAWTs, a design sometimes referred to as a Giromill utilizes a cycloidal blade system similar to those tested in the work above.

1.4 Research Aims/Present Work/Approach

Although cycloidal propellers have been tested in the past, several issues were encountered in these studies. All involved testing on large-scale models, and it remains uncertain how the design would translate to a MAV-scale vehicle. Furthermore, none of the previous studies had a comprehensive theory that matched well with their experimental results. Based on these problems, it became necessary to examine an MAV-scale cycloidal rotor in more detail.

The primary objective of this research was to determine if cycloidal propulsion is a viable means of propulsion for an MAV. A secondary objective was to develop the analytical tools necessary for predicting the performance of a cycloidal rotor and validate the tools with experiment.

The present work involved the characterization of a small-scale cycloidal rotor. A model rotor and test stand was designed and constructed. Performance of the rotor was studied by determining thrust and torque output as a function of blade pitch angle and rotational speed. A theoretical model was developed, showing thrust and torque levels that matched well with experimental results. The effect of the number of blades, blade pitch angle, and rotational speed on the rotor was examined. The direction of the thrust vector was found as a function of blade pitch angle. The test results were compared with the theoretical predictions. The efficiency of the test rotor was compared with that of a similar scale conventional rotor to determine the viability of cycloidal propulsion.

An investigation of the flow field around the model rotor was conducted. Pres-

sure measurements recorded incrementally around the rotor presented an acceptable quantitative picture of the downwash from the rotor.

A systems analysis was performed to determine if an MAV utilizing cycloidal propulsion is possible. A cyclo-MAV was designed and modeled in CATIA. Weights and constraints were applied to determine if the rotors could provide the thrust and control necessary for flight.

1.5 Thesis Outline

The thesis is organized into seven chapters. Chapter one provides a definition of the problem, previous work in the field, and the scope of the present work. The operating principles of the cycloidal blade system are described in Chapter two. Advantages and disadvantages of the system are also discussed. An analytical model developed for cycloidal rotor analysis in hover, is described in Chapter three. Chapter four provides a description of the model rotor and setup constructed for testing the cycloidal rotor concept. Testing procedures are explained as well. Experimental results are shown in Chapter five, and a comparison is made with predictions from the analysis. In Chapter six, a conceptual micro-air vehicle design utilizing cycloidal rotors is presented. A comparison is then made with a conventional rotary-wing MAV. Chapter seven summarizes the results of the present study and proposes future work that may be useful in understanding and implementing cycloidal propulsion.

Chapter 2

Operating Principles of Cycloidal Rotor

2.1 Operation

A cycloidal rotor consists of several blades that rotate about a horizontal axis that is perpendicular to the direction of flight (Fig. 1.9). Blade span is parallel to the axis of rotation. The pitch angle of each of the blades is varied such that it changes periodically about the airfoil quarter-chord as the blade moves around the azimuth of the rotor. Each of the blades produces a lift and a drag force. Blades at the top and bottom positions produce a vertical lifting force, while those at the left and right produce very little force because of their small angle of attack. When resolved into vertical and horizontal directions, as shown in Fig. 2.1, the sum of the horizontal components is zero, resulting in a net vertical thrust. Amplitude and phase of the oscillation in angle of attack may be changed, resulting in a change of the magnitude and direction of the net thrust vector of the rotor.

A unique and desirable characteristic of the cycloidal blade system is its ability to change the direction of thrust in any direction that is perpendicular to its axis of rotation. The enables a vehicle utilizing the system to take off and land vertically, to hover, and to fly forward or reverse by changing the direction of thrust.

For implementation on a vehicle, two cycloidal rotors would be necessary; one would be placed on each side of a fuselage containing drive components and control

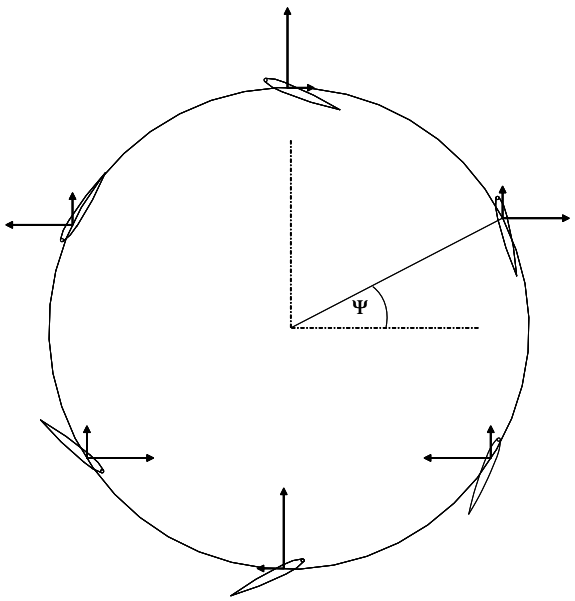

Figure 2.1: Cycloidal Rotor Thrust Vectors

mechanisms. Referring to Fig. 2.2, lateral motion and roll control is achieved through differential control of the magnitudes of the two thrust vectors. Yawing motion, as shown in Fig. 2.3, is accomplished through directional control of the thrust vectors. As both magnitude and direction of the rotor thrust vectors are controlled manually, maneuverability is limited only by the design of the control mechanisms. Unlike a helicopter, pitching is unnecessary in a cycloidal vehicle as propulsion is achieved by rotating the thrust vectors of the cycloidal blade systems. However, if desired, pitching could be accomplished either by an offset of the center of gravity from the rotational axis or the rotors or by adding a vertically thrusting tail rotor.

In forward flight, the blades trace out cycloids as they move about the rotor. These cycloids vary with advance ratio, defined as the ratio of the velocity parallel

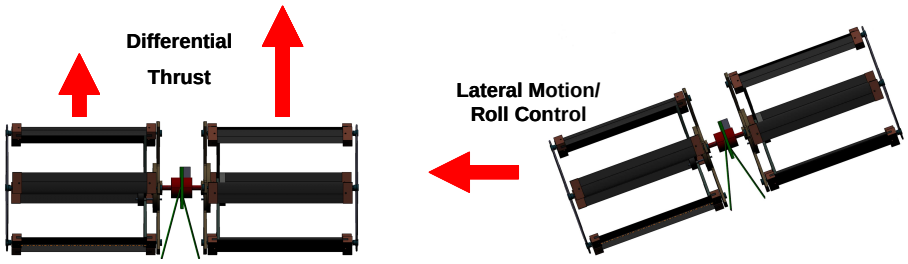

Figure 2.2: Lateral Motion and Roll Control for Cyclo-vehicle

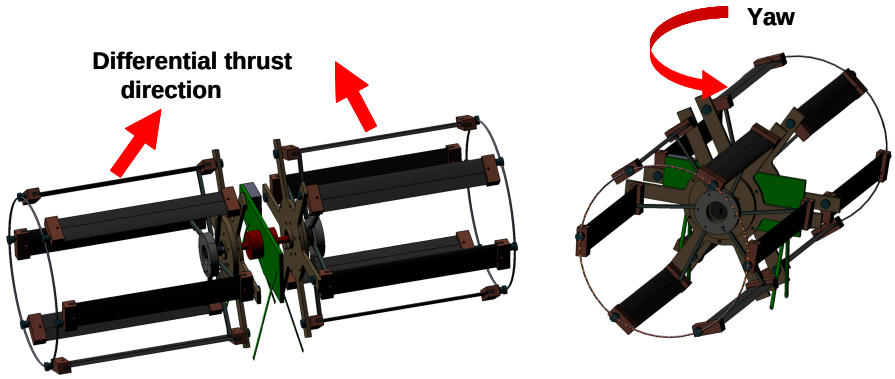

Figure 2.3: Yaw Control for Cyclo-vehicle

to the plane of the rotor to the tip speed of the rotor. Thus, different blade pitching motions are necessary as advance ratio changes to produce optimal thrust levels. At advance ratios below one, rotational speed has a greater impact on resultant velocity than forward speed. In this case, it is beneficial to keep blade pitching motions close to the tangent of the circular blade path. For advance ratios greater than one, forward speed has a more dominant effect on resultant velocity than rotating velocity, and blades should be kept with the leading edge in the direction of forward motion to achieve greatest efficiency.

2.2 Advantages

Cycloidal propulsion has a number of advantages over other flying configurations that make it attractive for use on a micro air vehicle. It provides the same hover capability as a conventional rotor. However, unlike a conventional rotor, the blades on a cycloidal rotor operate at a constant speed along the entire blade span, allowing all blade elements to operate at their peak efficiency. Inflow acting on each element is constant as well; thus, in the spanwise direction, inflow is uniform. Furthermore, as the direction of the thrust vector is varied mechanically, maneuverability of a vehicle using this type of rotor is limited only by the speed of the control mechanisms. This is of vital importance for a micro air vehicle, and provides a faster response than can be achieved by a conventional rotor. Cycloidal rotors typically operate at much lower rotational speeds than conventional rotors, and as such the acoustic signature should be significantly lower. For reconnaissance, this, too, is

essential. The greatest advantage of the design may be the possibility of greater thrust-to-power ratios than can be achieved by a conventional rotor. Previous work by [12] has claimed thrust-to-power ratios of two to three times greater than can be achieved from a standard rotor of similar dimensions. However, such a claim is based on many assumptions. For a micro air vehicle, where efficiency is of the utmost importance, this is quite noteworthy.

2.3 Disadvantages

However, cycloidal propulsion is not without its trade offs. The mechanism required to achieve the periodic pitch changes for each of the blades is by nature more complex than what is required for a conventional rotor. If the capability to vary the magnitude or direction of the pitch is necessary, as is needed for a vehicle, this complexity increases further. Moreover, although a simple four-bar mechanism can be used for blade pitch change in hover, it cannot provide the necessary changes in blade motion needed for forward flight. Consequently, the efficiency of a cycloidal rotor would decrease with advance ratio, in a manner similar to the loss of lift on the retreating side of a conventional rotor. To optimize a cycloidal rotor for all forward flight conditions, individual blade control would be needed.

The complex flow surrounding the rotor makes analysis of cycloidal propulsion difficult. Inflow through the rotor strongly affects the vertical component of the flow velocity with respect to blade chord line, and has a strong impact on thrust due to the interference between the blades. Furthermore, although Kim et al., have

performed a theoretical CFD analysis of the flow through a cycloidal rotor, no experiments have been conducted at this time to verify its accuracy [12].

Weight of the rotor is another shortcoming of the cycloidal configuration. The many components necessary for operation, i.e., multiple blades, bearings, and linkages, incur more weight penalty compared to a conventional rotor. It is not known at this time, however, whether the increase in weight offsets the gains in thrust and thrust-to-power for the configuration, and it is the purpose of this work to establish this relationship.

Chapter 3

Cycloidal Rotor Analytical Model

An analytical model of a cycloidal rotor, developed for the purpose of investigating the merits of the concept, is presented here. Specifically, the model predicts the magnitude and direction of thrust as well as power requirements of a cycloidal rotor in hover. The model is later applied to a rotor of the same dimensions as the experimental rotor constructed in the present work. A comparison of the experimental and theoretical results is presented in Chapter 5 in an attempt to validate the model.

3.1 Rotor Coordinate System

To calculate the performance of the rotor, the position of each blade must first be determined. By applying the motions of the pitch change mechanism, the angle of attack of each blade may be determined. Lift and drag forces are calculated. Downwash is determined from a modified version of momentum theory and used to calculate the induced angle of attack. An iterative procedure is then executed until convergence is achieved for lift and drag forces. The resulting forces from each blade are then summed to find the total vertical and horizontal forces for the rotor. The rotor is then rotated in an incremental amount and the process is repeated.

Fig. 3.1 shows the coordinate system used for the analysis. The azimuthal

position of the blade, Ψ, is measured counterclockwise from the negative z-axis. From Fig. 3.2, $\phi(s)$ is the phase angle of eccentricity, used to define the direction of thrust, is measured counterclockwise from the negative Z-axis. Blade pitch angle (θ) is measured with respect to the tangent of the blade's circular path. Velocities and forces are positive upward and in the direction of normal flight, as well in the direction of rotation and radially outward.

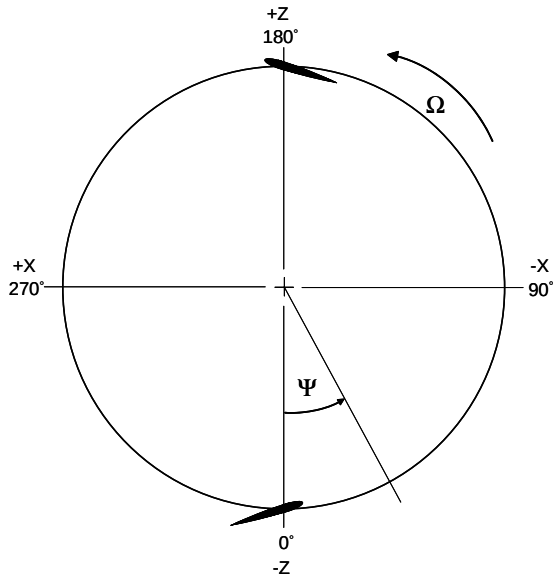

Figure 3.1: Coordinate System for Analysis

The coordinate system for the airfoil is shown in Fig. 3.3. The airfoil is represented as a line extending from the leading edge at $x = -1$ to the trailing edge at $x = +1$. The axis of rotation, or pitching axis, for the airfoil is located at point a. The airfoil may experience movement in the vertical direction, h, measured positive downward, or rotation about x=a, positive in the clockwise direction. A velocity v moves from left to right. An angle of attack α is defined as the angle between the

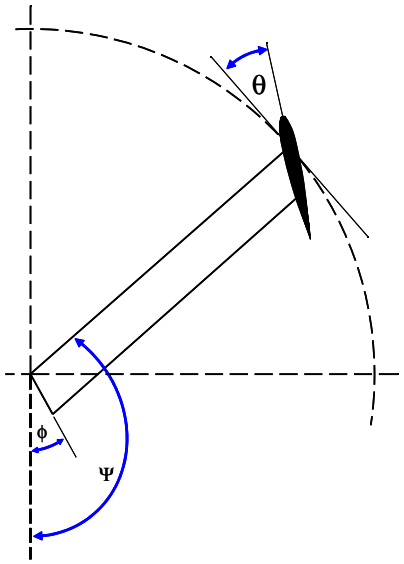

Figure 3.2: Cycloidal Rotor Pitch Definitions

velocity v and the instantaneous position of the airfoil, and provides a measure of the rotation about point a.

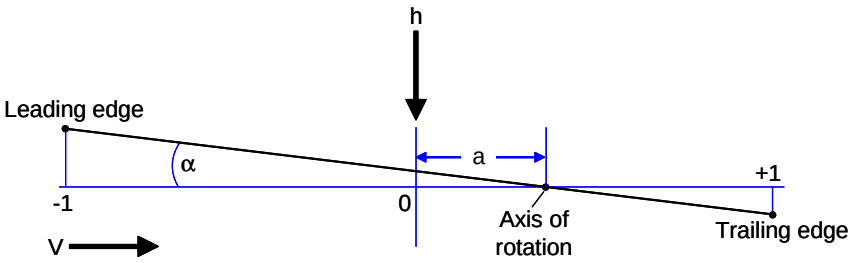

Figure 3.3: Airfoil Coordinate System

3.2 Forces and Moments

The blades on a cycloidal rotor experience a broad spectrum of unsteady effects as they rotate around the rotor. This includes the periodic oscillation in angle of

attack due to the pitch change mechanism, the effects of the previous blade wake, three-dimensional effects, and possibly dynamic stall. This last phenomenon has beneficial effects, such as the large overshoots in lift, drag, and pitching moments. However, it also creates large phase variations in the unsteady airloads experienced by the rotor blades, the values of which depend on the condition of the flow at that time - separated, stalled, or reattached. Under these conditions, quasi-steady aerodynamic theory may not be adequate. Therefore, unsteady aerodynamics are taken into consideration when developing the theory. As such effects are generally local, it was decided that the previous blade wake interactions could be neglected if blade spacing was far enough apart. Only the pitching oscillation experienced by the blade is taken into account when determining unsteady lift.

Initially, an attempt was made to use Theodorsen's theory for the aerodynamic cycloidal rotor theory. This approach provides the forced harmonic response of a 2-D airfoil undergoing harmonic oscillation or plunging motions in an inviscid, incompressible flow. In the case of a cycloidal rotor, the blades on the rotor undergo only a harmonic oscillation, and the solution is a simple transfer function between the forcing and the aerodynamic response.

The solution for this method, though, is dependent on the reduced frequency, a parameter used to describe the degree of unsteadiness of the flow, which comes from the non-dimensional Navier-Stokes equations. Reduced frequency is defined as

$$k = \frac{\omega b}{V} = \frac{\omega c}{2V} \tag{3.1}$$

where b is the airfoil semi-chord,

$$b = \frac{c}{2} \tag{3.2}$$

For $0 \leq k \leq 0.05$, unsteady effects may be neglected, and quasi-steady aerodynamics may be used. For $0.05 \leq k \leq 0.2$, the flow is unsteady, and the governing equations should include these terms. For $k > 0.2$, the flow is highly unsteady, and unsteady effects will begin to dominate the behavior of the airloads [26].

For the test rotor, the reduced frequency of the blade section is 0.167, in the unsteady regime. Note from Equation 3.3 that the reduced frequency simplifies to a geometric ratio independent of rotational speed and as such, its meaning is slightly ambiguous. One could conclude, for instance, that the rotor experiences unsteady flow at any rotational speed. However, if is difficult to justify this if the rotor is only spinning at one rotation per minute. Nevertheless, it does show that unsteady effects should most likely be accounted for in the analysis of the test rotor.

$$k \equiv= \frac{\omega c}{2V} = \frac{\omega c}{2\omega R} = \frac{c}{2R} \tag{3.3}$$

Although this method provides a relatively simple manner in which to include unsteady effects into the cycloidal rotor theory, there are some problems with this approach. The methodology used to arrive at the forces in the theory relies on a time domain formulation. Theodorsen's theory, on the other hand, is frequency based. To resolve these problems, Wagner's function was implemented in place of Theodorsen's function. Wagner's function is used in the solution for the indicial lift

on an airfoil undergoing an incremental change in angle of attack. The result for a step-change in pitch rate is given by the equation

$$\frac{\Delta C_p(\bar{x},t)}{q} = \frac{\delta(t)}{V}(1+2\bar{x})\sqrt{(1-\bar{x})\,\bar{x}} + (3\phi(s)-1)\sqrt{\frac{1-\bar{x}}{\bar{x}}} + 4\sqrt{(1-\bar{x})\,\bar{x}} \tag{3.4}$$

where $\delta(t)$ is the Dirac function and $\phi(s)$ is Wagner's function, which accounts for the shed wake. The variable s is the distance traveled by the shed wake, measured in semi-chords, and is given by

$$s = \frac{2Vt}{c} \tag{3.5}$$

for constant values of V. Fig. 3.4 presents Wagner's function. The infinite pulse at $s = 0$ is due to the apparent mass loading. It should be noted that in this derivation of the unsteady equations, Wagner's assumptions may not strictly apply to this problem. For instance, it is assumed that a planar wake leaves from the trailing edge of the airfoil. Although this may not be accurate for a conventional rotor, it has been demonstrated that his solution can be used to determine rotor forces. Thus, while the assumptions Wagner made may not be accurate for the cycloidal rotor, it is assumed that they can be used to obtain a satisfactory solution.

Equation 3.6 gives the variation in lift coefficient for a step change in angle of attack [26].

$$C_l(t) = \frac{\pi c}{2V}\delta(t) + 2\pi\alpha\phi(s) \tag{3.6}$$

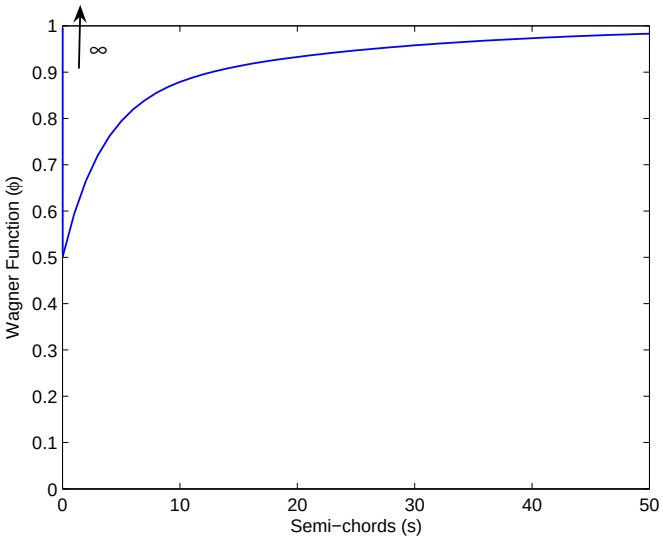

Figure 3.4: Wagner's Function

Once the response is found, the unsteady loads resulting from changes in angle of attack may be found through superposition of the responses, accomplished through a numerical solution to the convolution integral. Assuming the indicial response is known, the system output $y(t)$ is given by

$$y(t) = f(0)\phi(t) + \int_0^t \frac{df}{dt}\phi\left(t-\sigma\right)d\sigma \tag{3.7}$$

where $f(t)$ is the forcing function and $\phi(s)$ is the indicial response.

For this problem, the forcing function is the angle of attack of the blade, Wagner's function is the indicial response, and the lift is the output. Although Wagner's function is known exactly for incompressible flow, its formulation is not convenient for analytical work. Instead, an exponential approximation, provided by Jones [26], is used to simplify the problem. It has been shown to agree with the

exact function to within one percent.

$$\phi(s) \approx 1.0 - 0.165e^{-0.0455s} - 0.335e^{-0.3s} \tag{3.8}$$

With this in mind, the circulatory part of lift for a rigid airfoil starting from rest at t=0 in response to a variation in angle of attack is given by

$$L^c(s) = \frac{1}{2}\rho U^2 S C_{l_\alpha}[\alpha(0)\phi(s) + \int_{s_o}^{s} \frac{d\alpha(\sigma)}{ds}\phi\left(s-\sigma\right)d\sigma] \tag{3.9}$$

Including non-circulatory (apparent mass terms), the lift is given as

$$L(s) = C_{l_\alpha}\rho U^2 b[\alpha(0)\phi(s) + \int_{0}^{s} \frac{d\alpha(\sigma)}{ds}\phi\left(s-\sigma\right)d\sigma] + \pi\rho b^2\left(V\dot{\alpha} - ab\ddot{\alpha}\right) \tag{3.10}$$

per unit span, assuming V is constant, where a is the location of the pitch axis and b is the airfoil semi-chord [27]. For this case, the pitch axis is located at the quarter chord of the airfoil (a = -$\frac{1}{2}$). This result is then solved numerically for discrete values of time using a recurrence algorithm developed by [28].

Drag is calculated as the sum of the profile and induced components,

$$D = \frac{1}{2}\rho V^2 S\left(C_{D_o} + \frac{(C_L^c)^2}{\pi ARe}\right) \tag{3.11}$$

where C_{D_o} is the profile drag coefficient for the airfoil and C_{L^c} is the circulatory component of the unsteady lift found in Equation 3.9. Empirical data from Refs. [29] and [30] were used for the profile drag coefficients, as it has a strong dependence on Reynolds number and lift coefficient. The Oswald span efficiency factor is

represented as e, and a value of e=0.95 was assumed. Although this method of determining drag is not typical, it provides a manner in which to directly incorporate empirical data relevant to the present work. However, it must be understood that it has not been validated by other researchers.

The moment of the airfoil about its pitching axis, a, may be derived in a similar manner as

$$M_a = \pi\rho b^2 \left[-Ub\left(\frac{1}{2}-a\right)\dot{\alpha} - b^2\left(\frac{1}{8}+a^2\right)\ddot{\alpha}\right] \\ +C_{L_\alpha}\rho U b^2\left(a+\frac{1}{2}\right)\left[\alpha(0)\phi(s) + \int_{s_o}^{s}\frac{d\alpha(\sigma)}{ds}\phi\left(s-\sigma\right)d\sigma\right] \tag{3.12}$$

3.3 Motion of Pitch Mechanism

As explained earlier, the cycloidal blade system must provide both a lifting force and a propulsive force. This is achieved by varying the pitch angle of each blade in a periodic manner with respect to its location around the azimuth of the rotor. The equations above are dependent on α, $\dot{\alpha}$, and $\ddot{\alpha}$, which respectively represent the angle of attack, angular velocity and acceleration of the blade about its pitch axis (quarter-chord). The blade pitch angle can be idealized as a simple sinusoidal function, given by

$$\theta = -\theta_{max}\sin\left(\Psi - \phi\right) \tag{3.13}$$

where ϕ, the angle of eccentricity of the offset and Ψ, the position of the blade around the azimuth, are related to rotor speed by

$$\Psi = \Omega t \tag{3.14}$$

The angle of attack may be found by subtracting the induced angle of attack from the blade pitch angle.

$$\alpha = \alpha_{dw} - \theta = \alpha_{dw} + \theta_{max}\sin\left(\Omega t - \phi\right) \tag{3.15}$$

The angular velocity and acceleration, then, are the first and second derivatives of this function, respectively.

$$\dot{\theta} = -\theta_{max}\Omega\cos\left(\Omega t - \phi\right) \tag{3.16}$$

$$\ddot{\theta} = \theta_{max}\Omega^2\sin\left(\Omega t - \phi\right) \tag{3.17}$$

Although approximating angle of attack with a sinusoidal function provides an acceptable first approximation for the blade motion, it is not an exact solution, as the pitch change mechanism does not produce a pure sinusoidal variation in blade pitch angle. This difference also affects the angular velocity and acceleration, which influence the non-circulatory components of lift. Therefore, it is necessary to input the exact kinematics of the pitch change mechanism to achieve accurate results.

The mechanism in the experimental rotor utilizes a simple, passive four-bar mechanism to accomplish the blade pitch change. The various configurations and uses for this type of linkage system may be found in a wide variety of mechanics or kinematics textbooks [31]. Fig. 3.5 illustrates a generic four-bar linkage. Let L_1, L_2, L_3, and L_4 denote the lengths of the four linkages, with L_1 being the fixed linkage.

Angles θ_2, θ_3, and θ_4 give the angular positions of L_2, L_3, and L_4, respectively, and are measured counterclockwise from the horizontal plane. The diagonal, denoted by χ, runs from point B to point D. The angle from χ to L_3 is Ψ, while β is the angle from χ to L_1. L_2 is considered the driving linkage, and as such its angular position, θ_2, is known.[1]

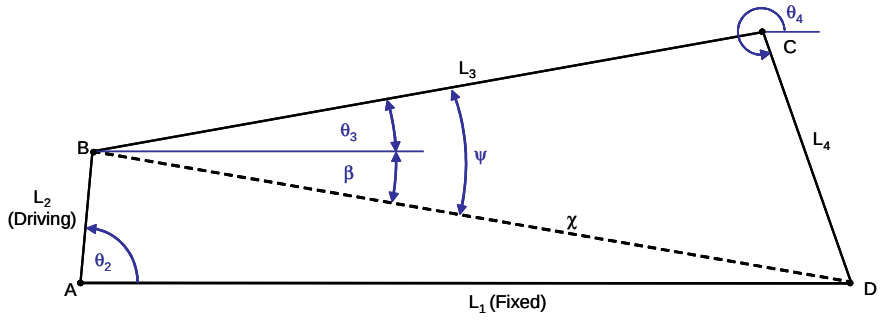

Figure 3.5: Generic Four Bar Linkage

First, consider triangle ABD. From the geometry,

$$\chi^2 = L_1^2 + L_2^2 - 2L_1L_2\cos\theta_2 \tag{3.18}$$

$$\frac{L_2}{\sin\beta} = \frac{\chi}{\sin\theta_2} \implies \beta = \sin^{-1}\left(\frac{L_2}{\chi}\sin\theta_2\right) \tag{3.19}$$

From triangle BCD,

[1]This is a simplifying assumption. For the case of the experimental mechanism, L_2 would be fixed and L_1, L_3, and L_4 would rotate around it. However, this would introduce a moving coordinate system that would make the problem unnecessarily more difficult. Therefore, for the sake of simplicity, the roles of L_1 and L_2 are reversed. This does not introduce any error into the problem, only a different perspective.

$$L_4^2 = L_3^2 + \chi^2 - 2L_3\chi\cos\Psi \implies \Psi = \cos^{-1}\left(\frac{L_4^2 - L_3^2 - \chi^2}{-2L_3\chi}\right) \tag{3.20}$$

$$\frac{L_3}{\sin\lambda} = \frac{L_4}{\sin\Psi} \implies \lambda = \sin^{-1}\left(\frac{L_3}{L_4}\sin\Psi\right) \tag{3.21}$$

There are two cases to be considered for the problem, illustrated in Figs. 3.6 and 3.7. In case 1, the line BC intersects line AD outside of AD; in case 2, the line BC intersects line AD inside the length OD. Each case requires a different approach to find θ_3 and θ_4.

For case 1:

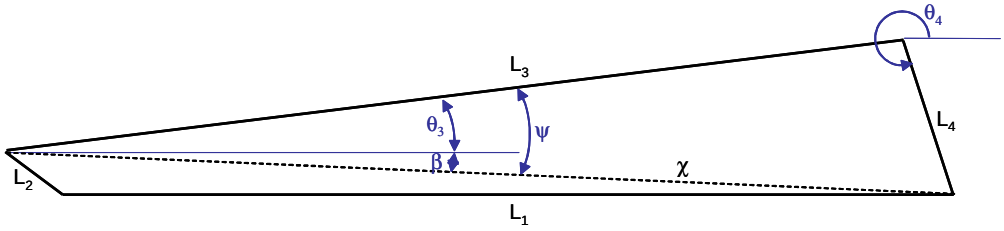

Figure 3.6: Case 1

$$\theta_3 = \Psi - \beta \tag{3.22}$$

$$\theta_4 = 2\pi - \lambda - \beta \tag{3.23}$$

For case 2:

$$\theta_3 = \Psi + \beta \tag{3.24}$$

$$\theta_4 = 2\pi - \lambda + \beta \tag{3.25}$$

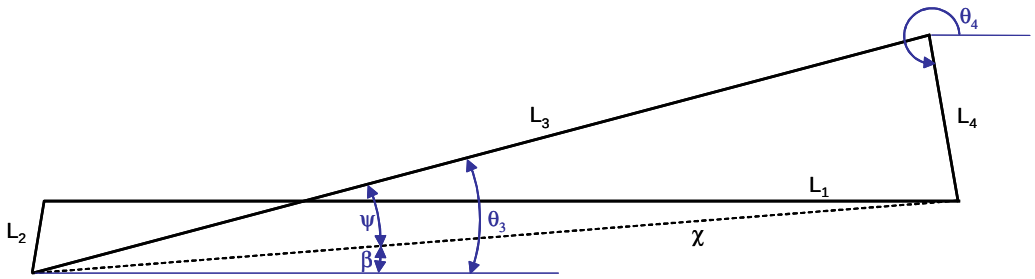

Figure 3.7: Case 2

Now that all the relevant angles in the linkage have been determined, the angular velocities and accelerations may be found. Since the linkages in the mechanism form a closed loop, if a vector is assigned to each link, the system may be represented in complex notation by the equation

$$r_1 e^{i\theta_1} + r_2 e^{i\theta_2} + r_3 e^{i\theta_3} + r_4 e^{i\theta_4} = 0 \tag{3.26}$$

where each linkage is represented as a vector with a magnitude r and direction. Recall that

$$\omega = \frac{d\theta}{dt} \tag{3.27}$$

and L_1 is fixed, $w_1 = 0$. Differentiating Equation 3.26, therefore, gives

$$ir_2\omega_2 e^{i\theta_2} + ir_3\omega_3 e^{i\theta_3} + ir_4\omega_4 e^{i\theta_4} = 0 \tag{3.28}$$

Because the linkages are expressed as vectors, separating the real and imaginary components give two equations:

$$ir_2\omega_2\cos\theta_2 + ir_3\omega_3\cos\theta_3 + ir_4\omega_4\cos\theta_4 = 0 \tag{3.29}$$

$$i^2r_2\omega_2\sin\theta_2 + i^2r_3\omega_3\sin\theta_3 + i^2r_4\omega_4\sin\theta_4 = 0 \tag{3.30}$$

Because the only unknowns are ω_3 and ω_4, solving Equation 3.30 simultaneously gives

$$\omega_3 = \frac{r_2\omega_2\sin(\theta_4 - \theta_2)}{r_3\sin(\theta_3 - \theta_4)} \tag{3.31}$$

$$\omega_4 = \frac{r_2\omega_2\sin(\theta_3 - \theta_2)}{r_4\sin(\theta_4 - \theta_3)} \tag{3.32}$$

The angular acceleration equations are found in a similar manner by differentiating the velocity equation. They are:

$$\alpha_3 = \frac{r_4\omega_4^2 + r_2\omega_2^2\cos(\theta_2 - \theta_4) + r_3\omega_3^2\cos(\theta_4 - \theta_3)}{r_3\sin(\theta_4 - \theta_3)} \tag{3.33}$$

$$\alpha_4 = \frac{r_3\omega_3^2 + r_2\omega_2^2\cos(\theta_2 - \theta_3) + r_4\omega_4^2\cos(\theta_4 - \theta_3)}{r_4\sin(\theta_3 - \theta_4)} \tag{3.34}$$

assuming the cycloidal rotor is not accelerating ($\alpha_2 = 0$). All angles, velocities, and accelerations are positive when measured counterclockwise. Thus, from the geometry of the linkage system, all the necessary terms may be determined as a function of θ_2. Fig. 3.8 compares the actual blade pitch angle (θ_4), velocity (ω_4), and acceleration (α_4) of the mechanism used in the experimental rotor to an ideal motion in which the blade pitch angle varies sinusoidally with a magnitude of 25°. Table 3.1 gives the lengths of the linkages.

Linkage	Length (in)
L_1	2.3307
L_2	0.180120
L_3	2.36935
L_4	0.4262

Table 3.1: Geometry of Linkages used on Experimental Rotor

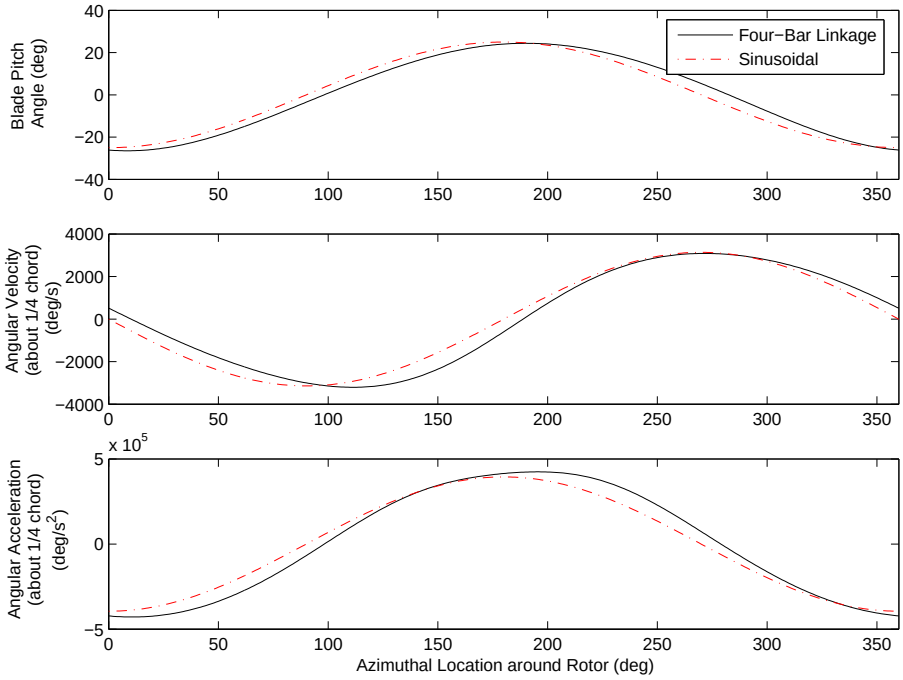

Figure 3.8: Actual and Ideal Motion of Blade Pitch Mechanism

Notice that the maximum pitch angles of the four-bar linkage are not exactly $\pm 25°$. The linkage has a slightly larger pitch angle at $\Psi = 0°$ ($\theta = -26.11°$), and a slightly smaller one at $\Psi = 180°$ ($\theta = 24.07°$). This difference between the upper and lower pitch angle escalates as the maximum pitch angle increases, and is an inevitable product of using a four-bar linkage. There is one benefit of this, however, in that as the blades move through $\Psi = 0°$, they experience a large downwash from the other blades, reducing the effective angle of attack at this position. The higher pitch angle at $\Psi = 0°$ decreases the effects of the downwash and maintains an acceptable angle of attack.

From Fig. 3.8, there is also a phase shift between the sinusoidal and actual blade motions. A closer examination of this in Fig. 3.9 shows a phase lag of approximately 10° between the location of the maximum blade pitch angle and the direction of the offset. The phase lag changes very slightly with the maximum blade pitch angle and is again a product of the four-bar linkage. The effects of this phase lag on thrust output will be examined in the experimental results.

3.4 Program Implementation

Implementation of the code begins by defining the two-dimensional lift-curve slope of the airfoil. The accepted value of 5.7 cannot be used in this case, as C_{l_α} deviates significantly from this value at low Re. Instead, empirical data from Refs. [29] and [30] were used, as in this body of research extensive testing was conducted on airfoils at Reynolds numbers below 70,000. The data used for the present work

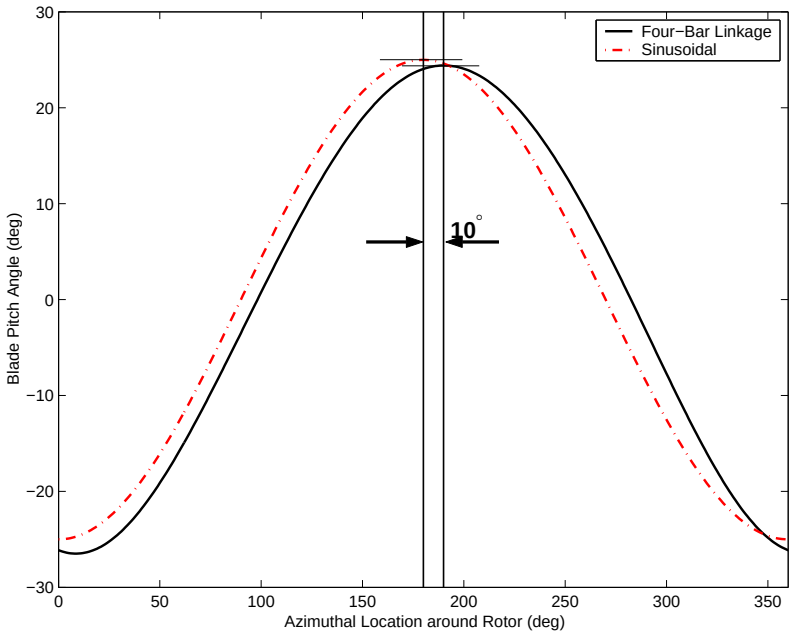

Figure 3.9: Phase Shift of Blade Pitch Angle

included lift and profile drag coefficients for an NACA 0012 wing with an aspect ratio of six at a Re of 20,700. Although the NACA 0010 airfoil was used for experiments in the current body of work, no known data for the NACA 0010 exists under the conditions tested. The use of the NACA 0012 data, however, should introduce only a small amount of error into the analysis.

Neglecting compressibility effects, the three-dimensional lift-curve slope may be calculated from the data:

$$C_{L_\alpha} = \frac{C_{l_\alpha}}{1 + \frac{C_{l_\alpha}}{\pi AR}} \tag{3.35}$$

If we consider only one position around the rotor azimuth, then as the system rotates the blades moving through that location will all be at the same pitch. This effect is similar to a cascade, or stationary array of blades, typically seen in axial

compressors. Fig. 3.10 shows an example of a rectilinear cascade and its geometric parameters [32]. Cascade aerodynamics take into account the interactions of each blade with its neighbors. For the present work, it must be determined what, if any, effect such interactions might have on the performance of a cycloidal propulsion system.

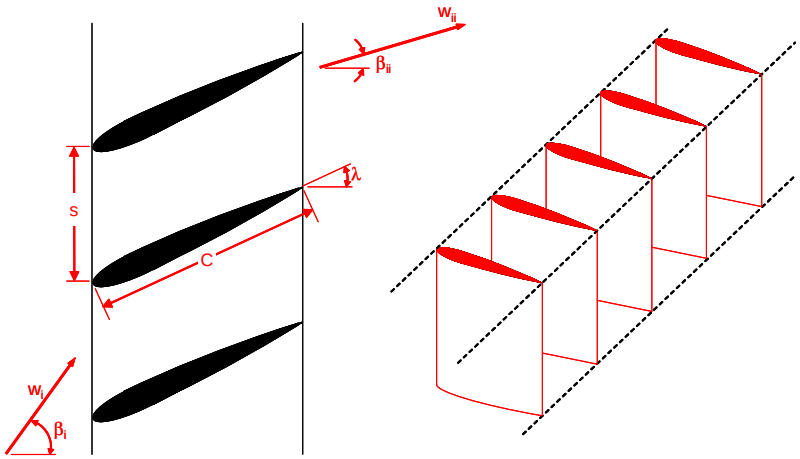

Figure 3.10: Geometry of rectilinear cascade

The ratio of chord, C, to blade spacing, s, is commonly referred to as the "solidity" of the cascade. Spacing effects have a strong effect on cascade performance, with pressure loss coefficients increasing rapidly with decreasing solidity and degrading performance, as shown in [33] and [34]. Compressors typically have solidities of 1.0 to 1.5. The experimental cycloidal rotor in the six-bladed configuration, on the other hand, has a solidity of 0.318. With only three blades, the solidity is half that value, or 0.159. Under these conditions the pressure loss coefficient is exceedingly high, and any cascade effects will be weak.

Reynolds number also has a significant impact on cascade performance. Refs.

[35] and [33] have shown that there is an increasing trend in loss coefficient with decreasing Reynolds number, with limiting blade-chord Reynolds numbers typically around 1.5 to $2.0x10^5$. At a Re of $2x10^5$, for example, pressure loss coefficients are typically near 0.02. However, at a Re of $2x10^4$, the maximum at which the cycloidal rotor has currently been tested, loss coefficients range from 0.2 to 0.4 at a solidity of 1.333 [35]. Obviously, the combined effects of low solidity and low Reynolds number would drastically reduce any cascade effects on the cycloidal rotor. Therefore, for this analysis the assumption will be made that they may be neglected.

Once the blade positions are determined from the linkage kinematics, the induced angle of attack and effective angle of attack are calculated. Referring to Fig. 3.11, on the upstream side of the rotor the local velocity on any blade element has a component $U_T = R\Omega$ tangential to the circular path swept by the blade as it moves around the rotor azimuth and a component $U_P = v_u$ normal to this blade path. On the downstream side, the local velocities are $U_T = R\Omega - w\sin\Psi$ and $U_P = v_d + w\cos\Psi$.

The induced angle of attack is found from the arctangent of the normal and tangential velocities, given by U_P and U_T, respectively.

$$\phi = \tan^{-1}\left(\frac{U_P}{U_T}\right) \tag{3.36}$$

The effective angle of attack experienced by the airfoil, then, is the difference between the blade pitch angle and the angle of attack induced by the downwash.

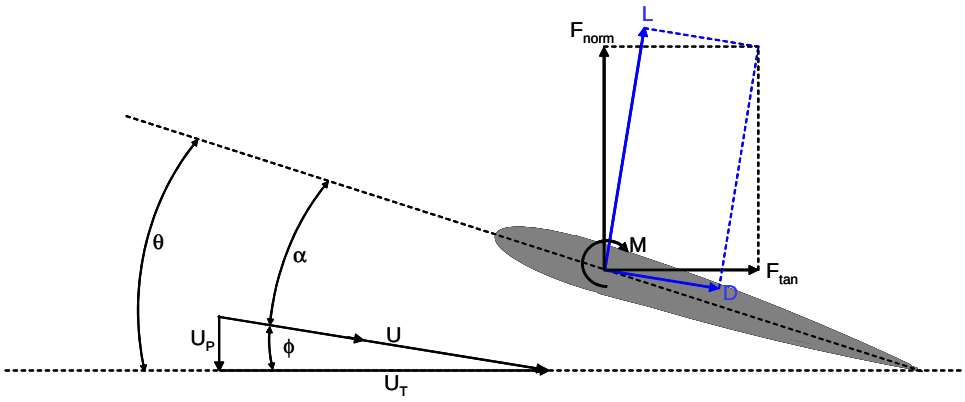

Figure 3.11: Blade Element

$$\alpha = \theta - \phi \tag{3.37}$$

Lift is calculated from Equation 3.10 and drag from Equation 3.11. In this case, U_R is the resultant velocity of U_T and U_P, given by

$$U_R = \sqrt{U_T^2 + U_P^2} \tag{3.38}$$

Once the lift and drag on each blade has been computed, they are resolved into forces in the x-z coordinate system of the rotor. From Fig. 3.11, lift and drag forces are first resolved into components normal and tangential to the cycloidal rotor motions:

$$F_{tan} = L\sin\phi + D\cos\phi \tag{3.39}$$

$$F_{norm} = L\cos\phi - D\sin\phi \tag{3.40}$$

The forces are now transformed into the x-z coordinate system. From Fig.

3.12, the transformation equations are found to be:

$$F_x = F_{norm}\cos(\theta_2 - 90) - F_{tan}\sin(\theta_2 - 90)$$

$$\Longrightarrow F_x = F_{norm}\sin\theta_2 + F_{tan}\cos\theta_2 \tag{3.41}$$

$$F_z = F_{norm}\sin(\theta_2 - 90) + F_{tan}\cos(\theta_2 - 90)$$

$$\Longrightarrow F_z = F_{tan}\sin\theta_2 - F_{norm}\cos\theta_2 \tag{3.42}$$

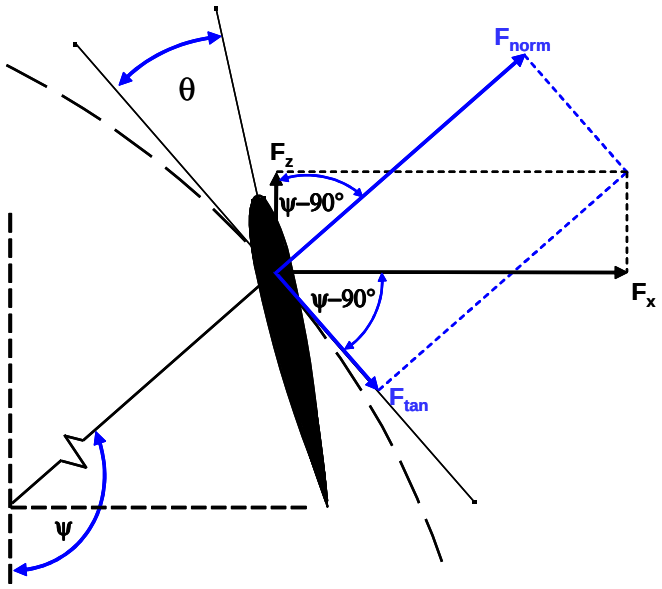

Figure 3.12: Force Components of X-Z System

Substituting Equations 3.40 and 3.40 into Equations 3.42 and 3.42, and including the effect of varying the angle of eccentricity, the forces in the x and z directions are given by

$$F_x = L\cos(\alpha_{dw} - \theta_2 + \phi) + D\sin(\alpha_{dw} - \theta_2 + \phi) \tag{3.43}$$

$$F_z = L\sin(\alpha_{dw} - \theta_2 + \phi) - D\cos(\alpha_{dw} - \theta_2 + \phi) \tag{3.44}$$

The total force in the x or z direction at any given time or position (Ψ), then, is the sum of the individual blade forces. By summing these total forces over an entire rotation, the average forces in the x and z directions may be determined.

Total thrust produced by the cycloidal rotor is given by

$$F_{res} = \sqrt{F_x^2 + F_z^2} \tag{3.45}$$

3.5 Streamtube Theory

The method of analysis employed to analyze the flow field around the cycloidal rotor is based on momentum theory, where the aerodynamic forces on the rotor are equated to the time rate of change in momentum through the rotor to determine the flow disturbance. This theory is based on the assumption that the induced axial velocity and the incidence angle between the chord line and the inflow are both constant along the blade chord. This method of analysis is similar to those used in the study of vertical axis wind turbines (VAWTs) [36]. Depending on the complexity of the problem and the accuracy necessary for the analysis, the models may further be classified into four types, shown in Fig. 3.13. Induced velocities are represented by u. The simplest model is the single streamtube, in which the rotor is assumed to act as a single actuator disk across which a pressure difference exists, in the same manner as in classical momentum theory. In the double streamtube model, the effects of the upstream wake on the downstream blades are taken into effect by

modeling the rotor as two actuator disks. For the case of the double streamtube models, the rotor is divided into multiple streamtubes, each of which has an induced velocity independent of the others.

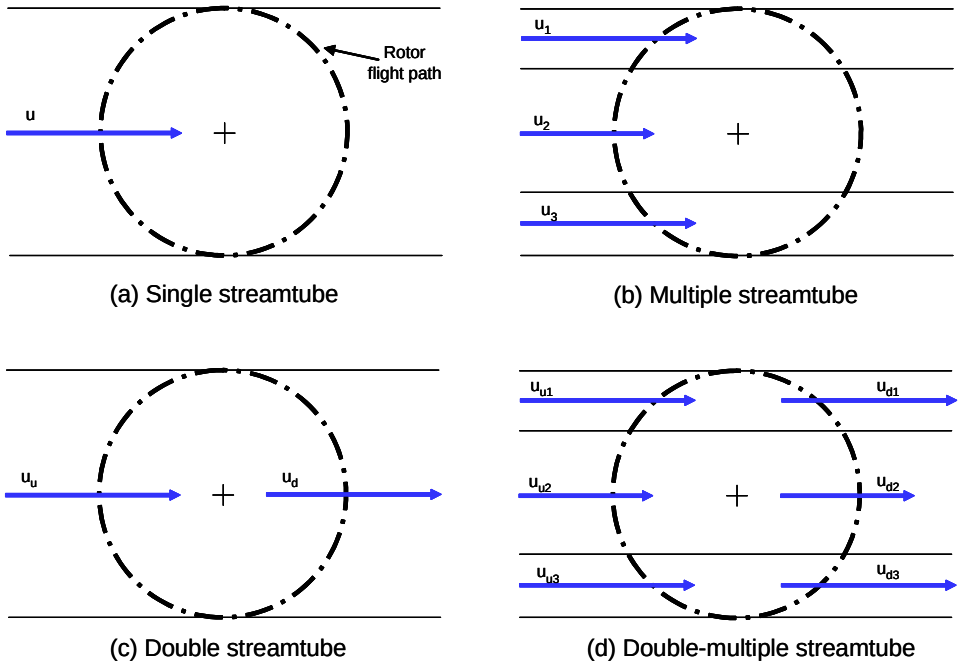

Figure 3.13: Streamtube models

For the analysis, an adaptation of double-multiple streamtube method was employed. In this model, the flow through the rotor is subdivided into a number of streamtubes, aerodynamically independent of one another and each with different induced velocities at the upstream and downstream halves of the volume swept by the rotor [37]. Each streamtube intersects the rotor twice, once on the upstream side and again on the downstream section, as shown in Fig. 3.14. At each of the intersections with the rotor circular path, the rotor is represented by an infinitesimally thin actuator disk. Across each of these disks exists a pressure difference

capable of generating axial momentum in the direction perpendicular to the disk. This momentum is equal to the force on the rotor divided by the area of the actuator disk. The induced flow through the actuator disks passes in the direction normal to the tangent of the rotor disk and is then deflected downward through the center of the rotor. It is assumed that the free stream velocity is achieved within the rotor, and the wake velocity of the upper actuator disk is used as the free stream velocity for the lower disk. Fig. 3.14 illustrates the flow model used for the analysis.

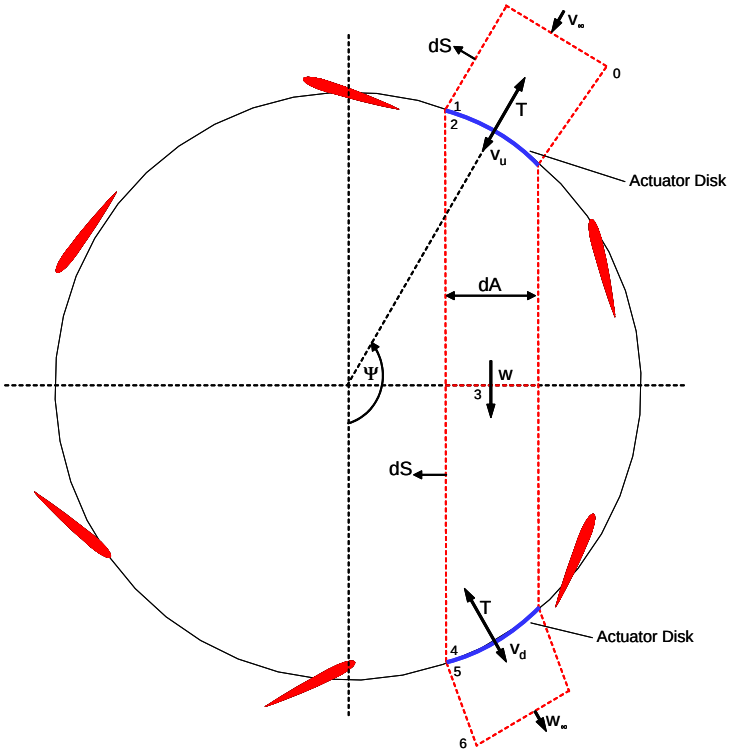

Figure 3.14: Flow model used for hover analysis

It is assumed that the flow through the rotor is one dimensional, incompressible, and inviscid. From the conservation laws of fluid mechanics, the net force on a fluid is equal to the time rate of change of momentum across the control surface (ac-

tuator disk). From Fig. 3.14, a control volume surrounding one streamtube and its wake has a surface area S. The unit normal area vector is represented by dS, and is normal to the surface of the control volume. Applying the principle of conservation of mass to the upper streamtube,

$$\dot{m} = \iint_3 \rho \vec{V} \cdot d\vec{S} = \iint_2 \rho \vec{V} \cdot d\vec{S} \tag{3.46}$$

With the assumptions of one dimensional, incompressible flow this reduces to

$$\rho dA_3 w = \rho dA_2 v_u \sin(\Psi - 90) \tag{3.47}$$

Applying the conservation of momentum, the thrust can be found as a function of the change in momentum out of the control volume:

$$T = \iint_3 \rho \left(\vec{V} \cdot d\vec{S}\right) \vec{V} - \iint_0 \rho \left(\vec{V} \cdot d\vec{S}\right) \vec{V} \tag{3.48}$$

For hover, the velocity in the far upstream of the rotor at cross section 0 is quiescent. Therefore, the second term on the right side is equal to zero. Thrust may then be written as

$$T = \dot{m} w \tag{3.49}$$

From the third conservation law of fluid mechanics, the principle of conservation of energy, the gain in energy of the fluid in the control volume is equal to the power consumed by the rotor:

$$Tv_u \sin(\Psi - 90) = \iint_3 \frac{1}{2}\rho\left(\vec{V}\cdot d\vec{S}\right)\vec{V}^2 - \iint_0 \frac{1}{2}\rho\left(\vec{V}\cdot d\vec{S}\right)\vec{V}^2 \tag{3.50}$$

with the second term on the right hand side again equal to zero due to the hover condition. This leaves

$$Tv_u \sin(\Psi - 90) = \frac{1}{2}\dot{m}w^2 \tag{3.51}$$

Combining Equations 3.49 and 3.51,

$$w = 2v_u \sin\Psi \tag{3.52}$$

If this relation is applied to Equation 3.47, it is apparent than the cross-sectional area of the far rotor wake must contract to one-half the area of the actuator disk, as shown in Fig. 3.15.

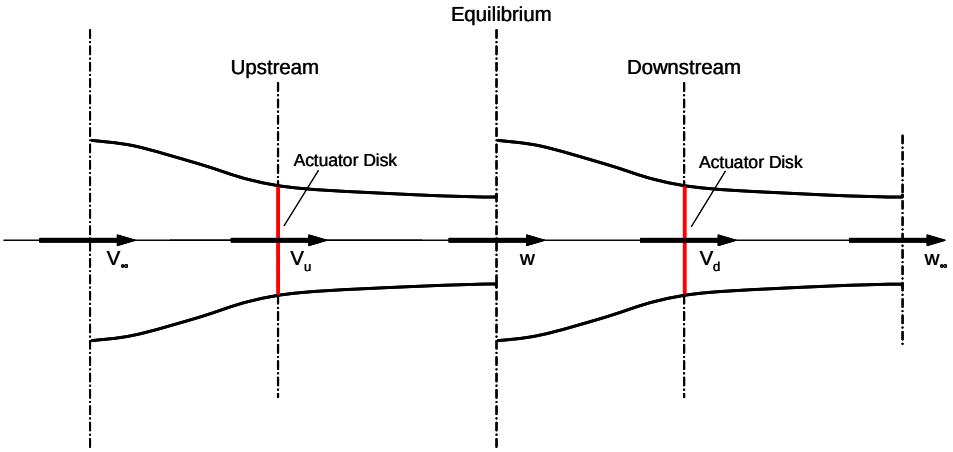

Figure 3.15: Streamtube replaced by two tandem actuator disks

Consider now the downstream half of the rotor. The velocity of the far wake

for the previous analysis now comes the far upstream velocity for this case. Applying the conservation of mass,

$$\dot{m} = \iint_6 \rho \vec{V} \cdot d\vec{S} = \iint_5 \rho \vec{V} \cdot d\vec{S} \tag{3.53}$$

which becomes

$$\rho dA_6 \left(w_\infty \sin\left(\Psi - 90\right) + w \right) = \rho dA_5 \left(v_d \sin\left(\Psi - 90\right) + w \right) \tag{3.54}$$

Conservation of momentum becomes

$$T = \iint_6 \rho \left(\vec{V} \cdot d\vec{S} \right) \vec{V} - \iint_3 \rho \left(\vec{V} \cdot d\vec{S} \right) \vec{V} \tag{3.55}$$

which reduces to

$$T = \dot{m} \left(w + w_\infty \sin\left(\Psi - 90\right) \right) - \dot{m} w = \dot{m} w_\infty \sin\left(\Psi - 90\right) \tag{3.56}$$

Note that the second term on the right hand side does not equal zero in this instance, as the far upstream velocity is equal to w. Conservation of energy for the lower actuator disk gives

$$T \left(v_d \sin\left(\Psi - 90\right) + w \right) = \iint_6 \frac{1}{2} \rho \left(\vec{V} \cdot d\vec{S} \right) \vec{V}^2 - \iint_3 \frac{1}{2} \rho \left(\vec{V} \cdot d\vec{S} \right) \vec{V}^2 \tag{3.57}$$

After inserting the values for the problem this reduces to

$$T \left(v_d \sin\left(\Psi - 90\right) + w \right) = \frac{1}{2} \dot{m} \left(w + w_\infty \sin\left(\Psi - 90\right) \right)^2 - \frac{1}{2} \dot{m} w^2 \tag{3.58}$$

$$2v_d = w_\infty \tag{3.59}$$

The induced velocity of the downstream actuator disk may now be determined:

$$T = \dot{m} w_\infty \sin(\Psi - 90) = \rho d A_5 \left(v_d \sin(\Psi - 90) + w\right) 2v_d \left(\sin(\Psi - 90)\right) \tag{3.60}$$

Rearranging and solving for v_d,

$$v_d = -\frac{1}{2} w \pm \sqrt{\frac{w^2}{4} - \frac{T}{2\rho d A_5 \cos\Psi}} \tag{3.61}$$

The induced velocities v_u and v_d are implemented into the program through an iterative scheme with the forces and moments until convergence occurs.

It should be noted that an assumption is made in this flow model that the two actuator disks in each streamtube produce the same thrust. As the lower actuator disk is in the downwash of the upper disk, this assumption is improbable. As such, it is recognized that this is a tentative flow model, and has not been validated experimentally.

3.6 Power

Power required by the rotor is a function of rotational speed and the torque about the axis of rotation. Torque, in turn, results from the profile and induced drag on the blades and an additional contribution associated with maintaining the blade oscillation, which is dependent on the kinetic energy of the vortex wake and

the work done by the propulsive force. From [38], the instantaneous rate at which work is done to maintain the oscillation of the airfoil is given by

$$\dot{W} = -\left(L\dot{h} + M\dot{\alpha}\right) \tag{3.62}$$

The total torque about the rotor axis, then, is given by

$$Q = \sum_{Numberofblades} F_{tan}R + \frac{M\dot{\alpha}}{\Omega} \tag{3.63}$$

Power required by the rotor is obtained by the following:

$$P = Q\Omega \tag{3.64}$$

It is important to note that the program in its present form may only be used to find forces and power requirements in hover. Wind forces and forward speeds are not included at this time. Should the concept prove to be feasible for use on a MAV, the program could easily be amended to include such details.

3.7 Computational Predictions

Fig. 3.16 shows the lift of one blade as a function of Ψ, its position around the azimuth of the rotor. There is a large phase shift associated with the four bar linkage pitch mechanism. At $\Psi = 180°$ the shift is approximately five degrees; at $\Psi = 0°$, lift has a leading phase shift of 15°. Furthermore, the magnitudes of thrust produced at these two positions is not equal; the blade produces slightly more thrust at $\Psi = 180°$.

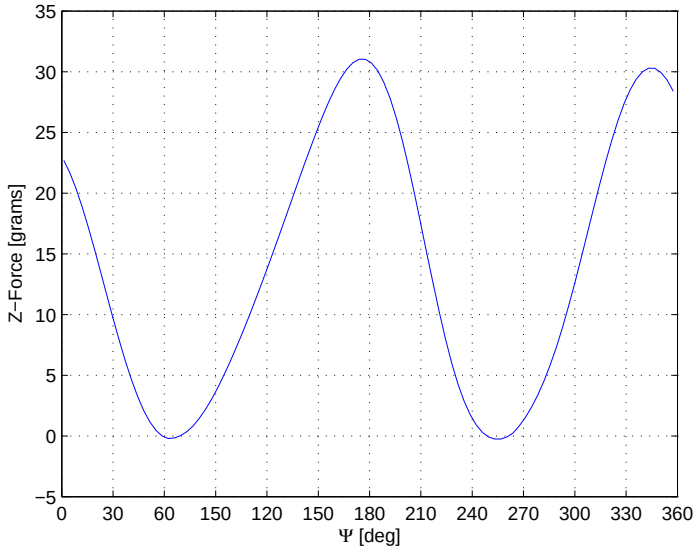

Figure 3.16: Lift of One Blade vs. Azimuthal Position

Fig. 3.17 shows the results of the model for a a six-bladed rotor with a maximum blade pitch angle of 30°. Thrust is proportional to the square of the rotational speed of the rotor, as expected. Fig. 3.18 shows that power required for a rotor in the same conditions is proportional to the cube of the rotational speed of the rotor.

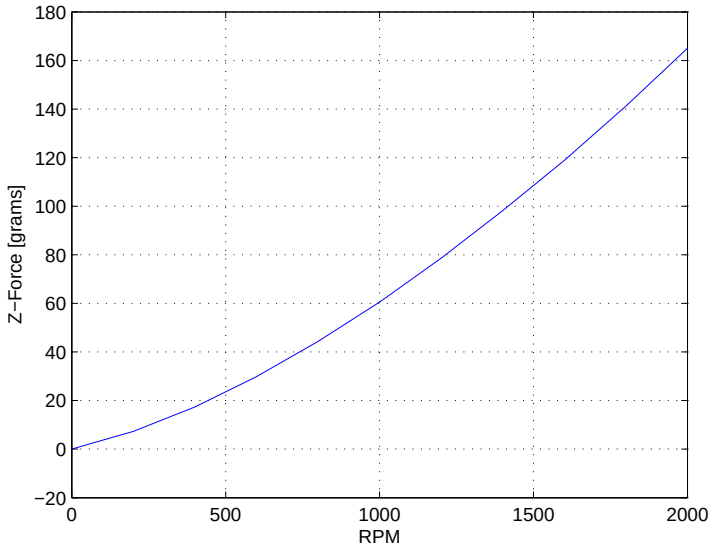

Figure 3.17: Z-Force for Six-Bladed Rotor, $\theta_{max} = 30°$

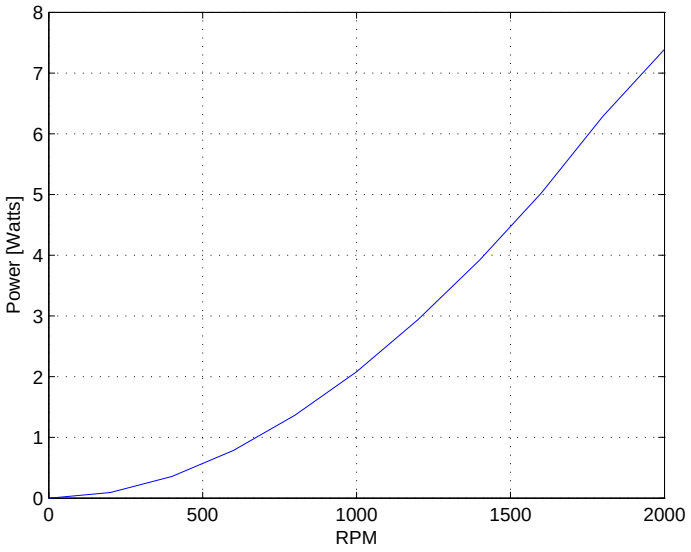

Figure 3.18: Power Required for Six-Bladed Rotor, $\theta_{max} = 30°$

Chapter 4

Experimental Rotor Design and Construction

4.1 First Generation Prototype

4.1.1 Rotor Design

The first cycloidal rotor constructed at the University of Maryland was designed and built by Belloli and Sirohi [22]. It consisted of a six bladed rotor with a diameter and blade span of six inches. Blades used a NACA 0010 airfoil profile, and had a one inch chord. Fig. 4.1 shows a picture of this model.

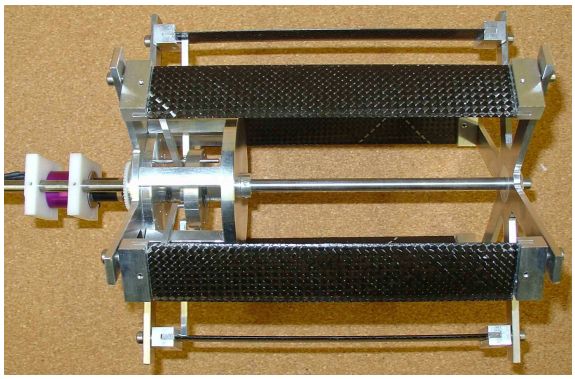

Figure 4.1: First Generation Experimental Rotor

An analytical study conducted by Ref. [22] to determine the optimum number of blades for the rotor, the results of which are shown in Fig. 4.2, determined that six blades would provide a significant increase in thrust over a rotor with two, three, or four blades. In addition, vibrations would be greatly reduced over the two and

three bladed configurations.

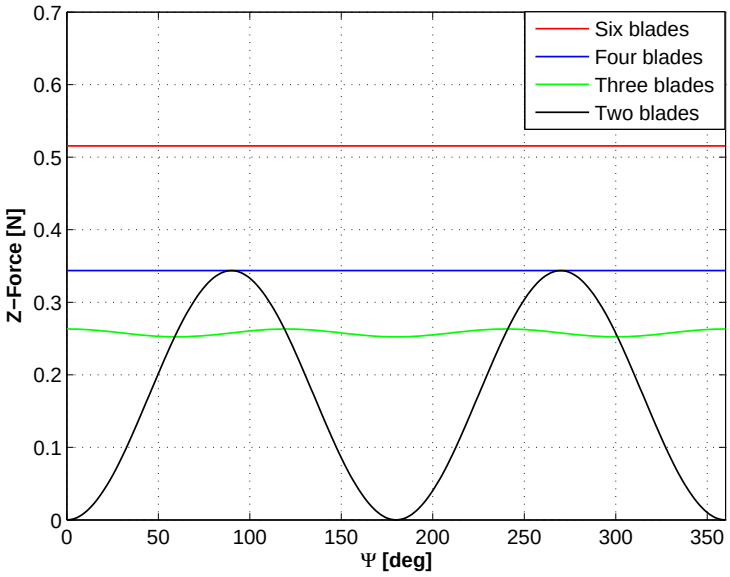

Figure 4.2: Variation of Thrust with Blade Number

The main structural elements of the design consists of two "star" end plates, to which each of the blades is attached. Connecting the star plates is a cage, which encloses the offset mechanism, and a shaft (Fig. 4.3). Together, these serve to maintain the alignment of the two end plates and to transmit the torque of the driven end to the free end. As will be discussed later, this design created some problems during testing, and a change was required to remedy the situation.

The mechanism devised for achieving the required blade pitch motions around the rotor is straight forward. As it is a passive system, the only power penalty required for its operation is the friction associated with its moving components. The mechanism consists of both fixed and rotating components. In Fig. 4.4, a shaft is offset from the center of rotation of the rotor. This component is fixed, and its

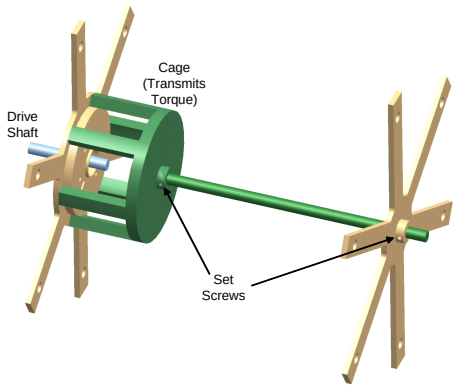

Figure 4.3: Structure of Cycloidal Rotor

orientation sets the direction of the thrust vector for the rotor. Attached to this piece is a bearing and a rotating disk, to which six linkages are attached. Each of the linkages connects to the trailing edge of one of the blades. Together, the system comprises a crank-rocker type four-bar linkage, which is used to accomplish the required change in blade pitch angle (Fig. 4.5).

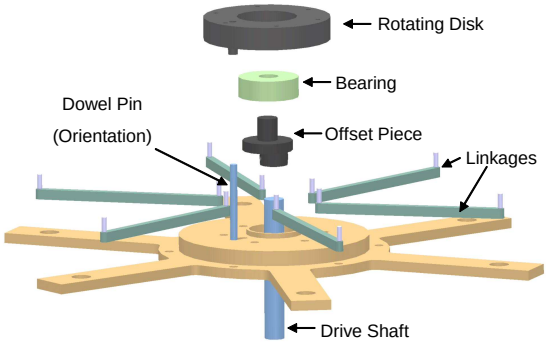

Figure 4.4: Offset Mechanism Components

The mechanism was originally designed such that the blade pitch angle would vary periodically between $\pm 10°$. The magnitude of the blade pitch angle is depen-

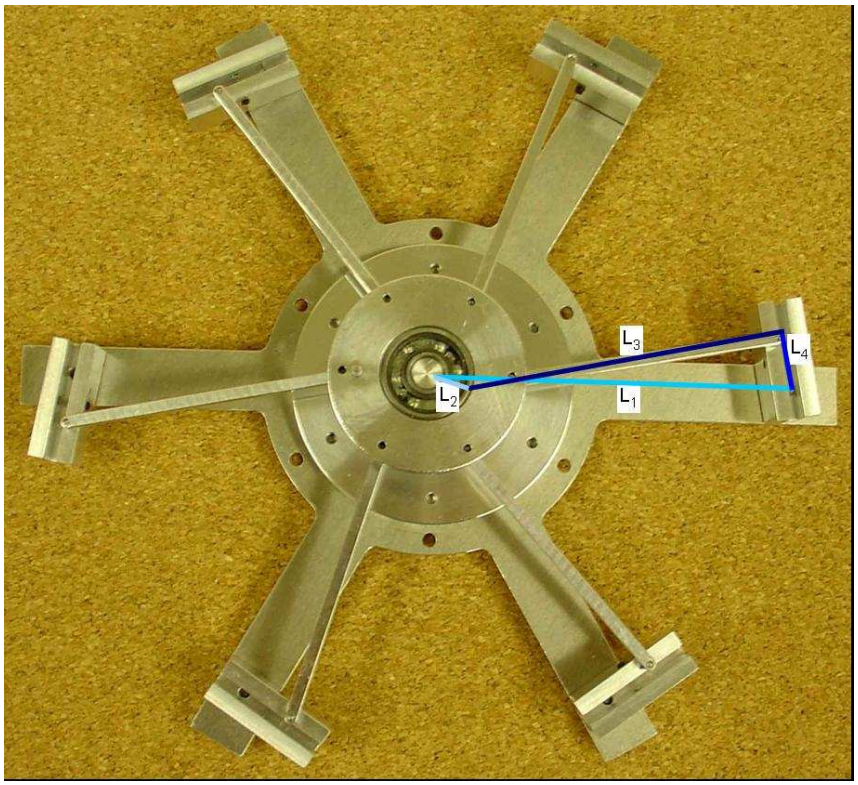

Figure 4.5: Offset Mechanism Four Bar Linkage

dent on the distance between the offset shaft and the rotational axis of the rotor; this is equivalent to linkage L_2 in the four-bar linkage mechanism in Fig. 4.5. Thus, with this setup a new part with a different offset must be machined for each blade pitch angle that is to be tested.

A dowel pin, attached to the disk in Fig. 4.6, moves in a slot machined in the driven end plate. This prevents parasitic motion and maintains a constant orientation for the maximum blade pitch angle.

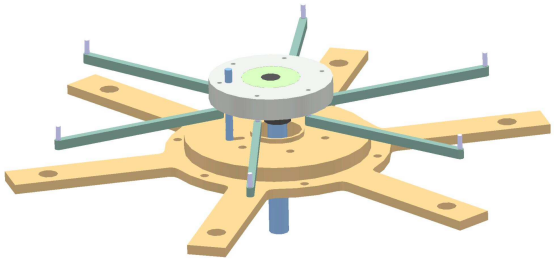

Figure 4.6: Offset Mechanism

The blades for the cycloidal rotor are constructed of carbon fiber composite enclosing a foam core (Fig. 4.7). Because of the constraints that they operate effectively at both positive and negative angles of attack, the symmetric NACA 0010 profile was used for the airfoils. This airfoil had a profile thin enough to provide adequate performance at low Reynolds numbers, but still provided the necessary stiffness to resist centrifugal loads.

To fabricate the blades, a matching mold set for a NACA 0010 airfoil with a span of six inches and a chord of one inch was first machined out of aluminum (Fig.

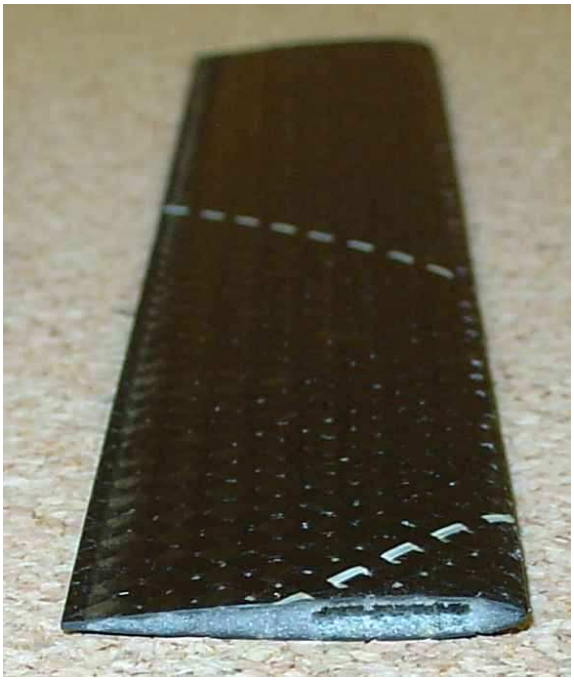

Figure 4.7: Blade Construction

4.8). A form core, inserted in the mold, was first cured at 180° C to harden the foam. The leading and trailing edges were then filed to the correct blade dimensions and to achieve a smooth profile.

Pre-impregnated carbon fiber was then wrapped around the foam core and inserted in the mold, which is cured for one hour at 177° C. The blade is then removed and sanded to the correct dimensions. Although somewhat labor-intensive, this design provides a lightweight blade capable of resisting the considerable transverse centrifugal forces inherent to the cycloidal rotor. An aluminum extension inserted into each end of the blade (Fig. 4.9), fits in a fastening block at each end of the blade. This allows the blades to easily be removed from the rotor to service the offset mechanism or for repair purposes.

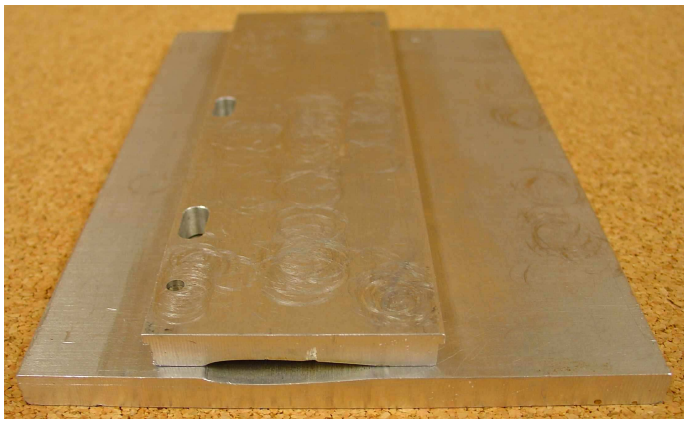

Figure 4.8: Blade Mold

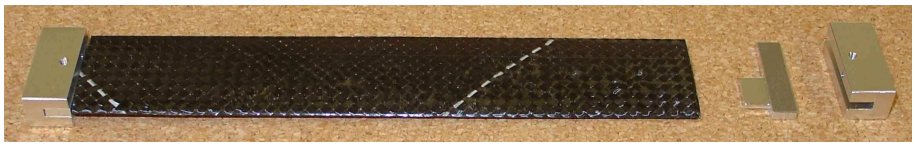

Figure 4.9: Exploded Blade

4.1.2 Test Setup

The rotor was driven by a brushless Hacker Motor, model B20 36S, shown in Fig. 4.10 [39]. Although the electronics required to operate them are slightly more complex, brushless motors are more efficient than their DC counterparts, and provide a great deal of torque for their small size. A set of brass gears, used for longevity and smooth operation is used to drive the propeller at one-quarter the speed of the motor.

Figure 4.10: Brushless Hacker Motor

The brushless motor requires a pulse-width modulated (PWM) wave input for operation. Therefore, a speed controller in conjunction with a micro precision pulse generator/servo tester is used to operate the motor. Both of these are readily available for use in radio-controlled vehicles. The speed controller is powered by a DC power supply. The servo tester is used to vary the speed of the motor by varying the duty cycle of the PWM wave.

The force balance constructed by Belloli and Sirohi placed the rotor in a cantilever configuration and used a load cell to measure thrust. From Fig. 4.11, thrust

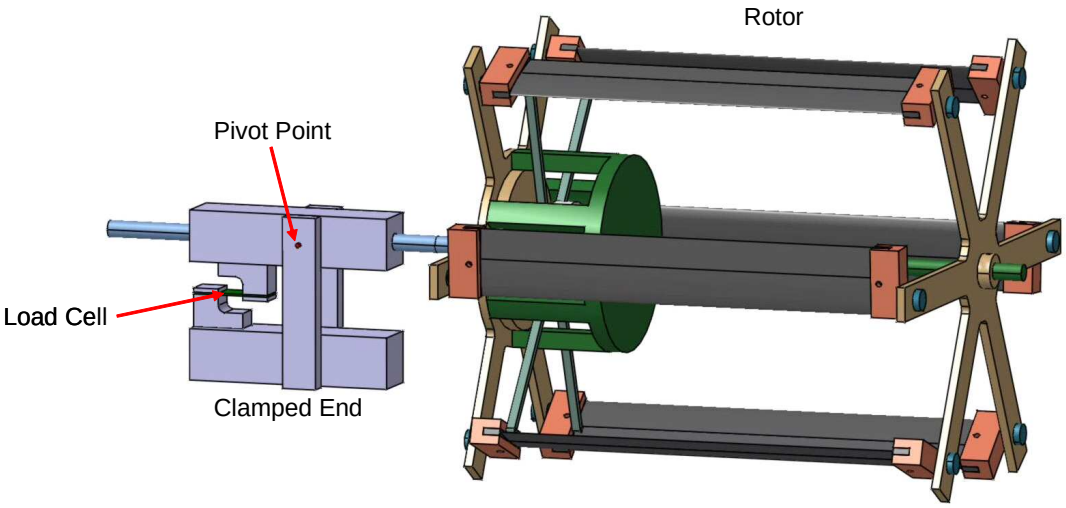

Figure 4.11: First Generation Test Setup

and vibration in the rotor causes the load cell to deflect in an S-shape, from which the thrust can be found if the calibration for the load cell is known. A Hall sensor was used to measure rotational speed, and a circuit was devised to measure voltage and current requirements of the system, used to determine power consumption. However, this method of finding power is dependent on the efficiency of the motor, and as such will change if a different motor is used. Moreover, it is accurate only if the voltage and current are in phase with one another, and it is unknown if this was the case for the setup.

4.1.3 Problems

Preliminary tests measured thrust, voltage, current, and rotational speed. Data was acquired using a National Instruments PCI-6031E 16-bit DAQ card in conjunction with a Matlab program [40, 41]. Thrust and torque measurements were

first run through a Vishay 2311 Signal Conditioning Amplifier [42], with an excitation voltage of +10V and a gain of 750. The signal from the Hall sensor was through a feed-through module with no gain. Data processing was performed in Matlab.

After initial testing was conducted with the first generation rotor and test stand, a number of issues were discovered that precluded further use.

(a) The rotor experienced excessive vibrations, an order of magnitude larger than the measured values of thrust. Operation near the natural frequency at 800 RPM was particularly detrimental to the rotor. A possible misalignment of some of the components connecting the two star plates may have contributed to the vibrations. Weight imbalance could also be a possible source of the vibrations, although all components were weighed and balanced to within 0.02 grams. Any imbalance in the components would pose a considerable challenge in measuring accurate thrust levels, as it would lead to whirling in the same direction as the thrust produced by the rotor. The cantilevered configuration of the test stand exacerbated the problem.

(b) Testing conducted on the rotor to determine its wake structure, the results of which are further discussed in Chapter 5, demonstrated a loss of lift over the outer third of the rotor. Further investigation led to the conclusion that the cantilever setup and excessive rotor vibrations were the source of the problem. Both ends were then clamped to finish the wake testing; however, this precluded any further thrust or power measurements while in that configuration.

(c) In the first generation rotor, the cage and shaft used to transmit torque to the

free end plate of the rotor was necessary, as there was possibility of incorporating a continuous shaft through the entire rotor. However, the configuration led to some problems. The shaft connecting the cage and the free end plate was fastened using set screws. During testing, it became apparent that the free end plate could twist with respect to the fixed end; that is, the blades were no longer parallel to the rotational shaft. The origin of the problems was the set screws that were used to maintain alignment of the configuration which did not possess the necessary strength to prevent movement of the components. Although steps were taken in an attempt to remedy the problem, no acceptable solution was found.

(d) It was determined that the length and configuration of the linkages were not correct to achieve the desired $\pm 10^\circ$ blade pitch angles. Instead, the rotor achieved pitch angles of approximately 0° at $\Psi = 0^\circ$, and $+20^\circ$ at $\Psi = 180^\circ$. New linkages of the correct length were made before further testing.

(e) The linkages were originally held in position on the rotating disk by dowel pins. During testing, the pins would at times slip out of the rotating disk, causing a large imbalance in the rotor, necessitating the load cell to be recalibrated.

(f) The pitch change mechanism, while mechanically simple, was fixed such that only one blade pitch angle could be tested. A change in the maximum blade pitch angle required machining a new offset piece for each angle to be tested and a complete disassembly of the rotor to install the component. This not only required a great deal of time, but increased the possibility of an error

occurring during reassembly.

(g) The rotor retained a great deal of friction among components. Although the friction was due to number of design elements, the dowel pin used to maintain orientation of the thrust vector was a contributing factor. Also at issue were fastening blocks used to grip the blades at each end; over time, these began to rub against the end plates, causing damage and greatly increasing friction in the rotor.

(h) As previously mentioned, the cantilever setup used for testing was not conducive to accurate thrust measurements. The setup exacerbated any vibrations in the rotor. The method of determining power consumption, through the measurement of voltage and current, also has a number of issues. This method determines the total power consumed, including the losses from the motor inefficiency and from the friction of the mechanical components in the rotor.

These problems and concerns led to some question about the validity of the data acquired during initial testing. As a result, a new rotor and test stand were designed and constructed in an effort to eliminate those problems associated with the first rotor. The new setup was also designed to provide greater flexibility for testing, allowing for a more accurate characterization of the cycloidal rotor.

4.2 Second Generation Prototype

4.2.1 Design

The second cycloidal rotor constructed at the University of Maryland, as part of the present work, retained much of the design of the first rotor. However, a number of changes were made to resolve the shortcomings of the previous generation.

To ensure that the components remain properly aligned, and blades remain parallel to the axis of rotation, the cage and shaft used on the first generation rotor were eliminated. In its place, a one-inch diameter stainless steel tube connects the two end plates and provides the rigidity necessary to transmit torque between them. Furthermore, it eliminates the blade skew that occurred previously. Two bearings on each end plate ensure smooth, frictionless rotation about the continuous non-rotating center shaft, which continues through both ends of the test stand in a fixed-fixed configuration.

The changes made in the design necessitated moving the pitch change mechanism outside the rotor, allowing for much more straightforward manipulation and modification of the mechanism. A new pitch change mechanism, shown in Fig. 4.12, was designed that provides infinitely variable pitch angles from 0° to 40°. Referring to Fig. 3.5, this change in pitch is accomplished by effectively changing the length of linkage L_2. As one of the primary objectives of the experiment is to determine the change in thrust as a function of blade pitch angle, the new design not only makes this possible, but minimizes the time required to do so as it can be accomplished without disassembling the rotor and without machining new components.

Figure 4.12: Variable Pitch Change Mechanism

The dowel pin/slot combination used previously to maintain the orientation of the thrust vector not only added a considerable amount of friction, but increased overall weight to the design as well. In its place, one of the linkages that connects to the rotating disk was placed at a fixed orientation. This design minimizes weight increase while eliminating friction associated with the dowel pin and slot.

The previous problem of the linkages separating from the rotating disk during operation was remedied by using shoulder screws to fasten the linkages to the rotating disk. New linkages were machined such that the blade pitch angle was 0° when pitch offset was zero.

In an effort to minimize vibration in the design, all components were weighed and balanced within 0.01 grams. Unnecessary weight of the system was reduced to minimize inertial forces.

4.2.2 Test Setup

A new test setup was also constructed to increase fidelity of the acquired data and to provide additional functionality. Two TBS-5 load cells from Transducer Techniques were included for better accuracy [43]. Each has a load capacity of five pounds and a rated output of 2mV/V. Figs. 4.13 and 4.14 illustrate the improved stand. The non-rotating shaft on which the rotor is mounted runs through vertical plates at above each load cell. These plates are mounted on linear slides, preventing horizontal motion and minimizing friction. The plates are attached to the load cells, which are, in turn, attached to the base. An RTS-25 torque cell, also from Transducer Techniques, is mounted on one of the vertical plates and measures the torque produced by the system [43]. The torque cell has a capacity of 25 oz.-in. and a rated output of 1.5 mV/V. By mounting the torque cell directly to the second plate rather than having it support the non-rotating shaft, all bending loads acting on torque cell are removed. Torque is transmitted from the rotor to the motor, which is attached to the non-rotating shaft. The shaft, in turn, is attached to the torque cell. A Hall switch measures rotational speed of the rotor. The Hall switch is more robust than the linear Hall sensors used previously. Completed, the second-generation setup is capable of measuring thrust, torque, and rotational speed with a high degree of accuracy.

A range of tests were performed to characterize the performance of the rotor. Measurements were taken at blade pitch angles of 10, 20, 30, and 40° for rotational speeds ranging from 0 to 1200 RPM. Although the rotor is capable of higher speeds,

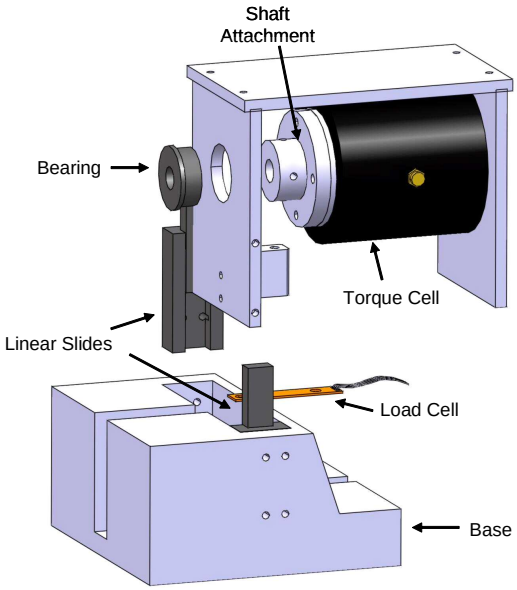

Figure 4.13: Test Stand Base

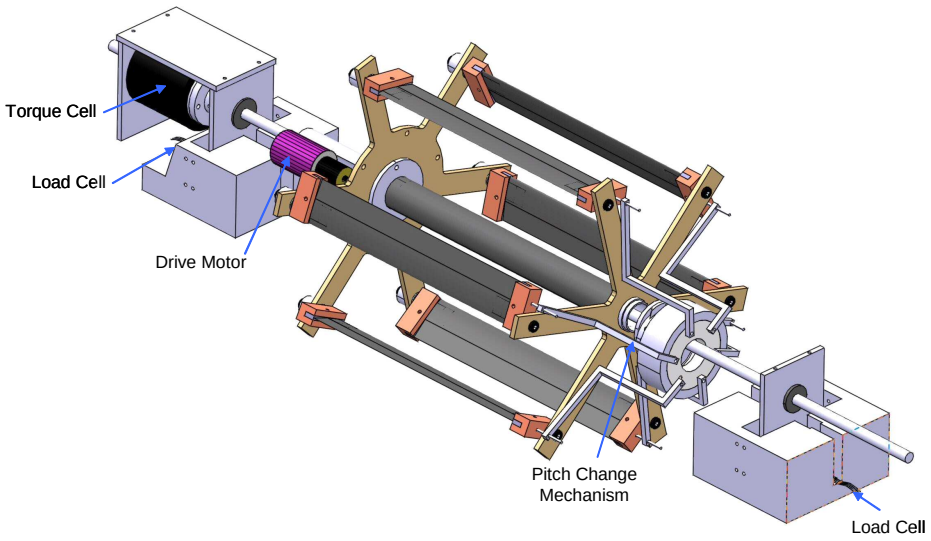

Figure 4.14: Generation Two Test Setup

testing was stopped at this point to prevent the transient torque loads from damaging the torque cell. The tests, first conducted with six blades, were repeated with three blades to determine the relationship between the number of blades and the output of the rotor.

A series of tests were also performed to determine the effect of blade pitch angle on the direction of the resultant thrust vector. Measurements were recorded for blade pitch angles ranging from 0 to 40° and eccentricities, ϕ, from -50 to 50°. Rotational speed was held constant at 800 RPM.

In order to determine the breakdown of power for the rotor, tare tests were performed with all blades removed from the rotor. Testing was conducted for blade pitch angles from 0 to 40°, with rotational speeds ranging from 0 to 1200 RPM.

Data for all testing was acquired using a National Instruments PCMCIA-6062E 12-bit DAQ card in conjunction with a LabView program written by Sirohi [40]. Thrust measurements were first run through a Vishay 2311 Signal Conditioning Amplifier, with an excitation voltage of +10V and a gain of 750. A filter of 10 Hz was applied. Torque was measured with a SCC-SG24 module, with an excitation voltage of 10V and a gain of 100. The signal from the Hall switch was recorded through a feed-through module with no gain. The program recorded thrust from the two load cells, torque from the torque cell, and rotational speed from the Hall switch. Data processing was performed in LabView.

Additional experiments were also performed to determine the downwash distribution below and obtain a quantitative picture of the flow around a cycloidal rotor. Static and dynamic pressure measurements were measured using pitot-static

probes from United Sensor Corporation (Fig. 4.15) [44].

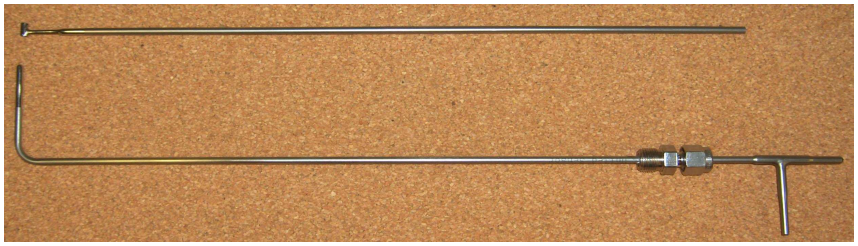

Figure 4.15: PS Probe, Kiel Probe

A Setra differential pressure transducer (12V excitation, 0-50 Pa range) was used to compute the dynamic pressure [45]. Pressure measurements were recorded at one-inch increments in both the x and y directions. The measurements were then repeated at locations of $\frac{1}{2}$, 3, 6, and 9 inches below the rotor. Rotational speed was kept constant at 1100 RPM. Vertical movement was achieved by mounting the probes on a Mitutoyo height gauge, with a precision of ± 0.001 inch. Movement in the x and y directions was accomplished by mounting the height gauge to a two degree-of-freedom x-y positioning stage driven by stepper motors [46]. Control of the motors was accomplished through CNC Flashcut software; this allowed for movements in the x and y directions with a precision of ± 0.001 inch.

Data for the wake measurements was acquired using a National Instruments PCI-6062E 12-bit DAQ card in conjunction with a Matlab program [40, 41]. The signal from the Hall sensor was sent through a feed-through module with no gain. All data processing was performed in Matlab.

Initial testing was performed on the first generation rotor in the cantilevered condition. Coordinate axes used in the measurement are defined in Fig. 4.16.

Measurements were recorded from x=-6 to x=6 and y=-4 to y=4. The tests were later repeated with both ends of the rotor in a clamped condition. A Kiel probe from United Sensor Corporation, shown in Fig. 4.15, was used to measure dynamic pressure in place of the pitot-static probe. Kiel probes are insensitive to angle, reading total pressure over an entry cone angle of 45° or more, making them ideal for an application such as this where exact flow direction is unknown [34].

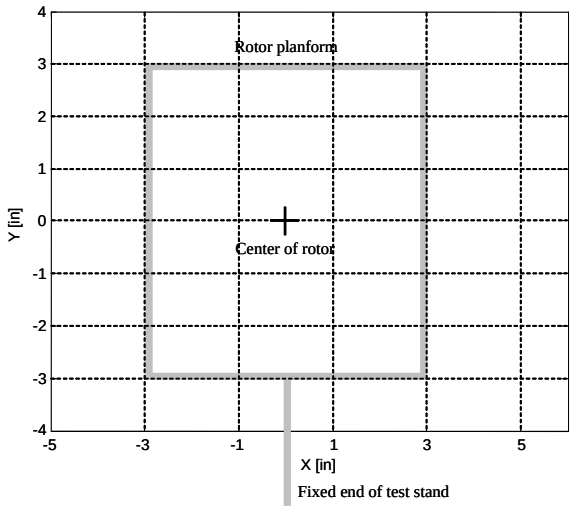

Figure 4.16: Pressure Measurement Coordinate Axis Definition

Measurements were then taken of the flow cross-section. The Kiel and static pitot probes were located at the center of the blade span, and pressure measurements were recorded in the x and z directions in one-inch increments from x=-6 to x=6 and z=-7 to z=7. Fig. 4.17 defines the coordinate axes for the testing.

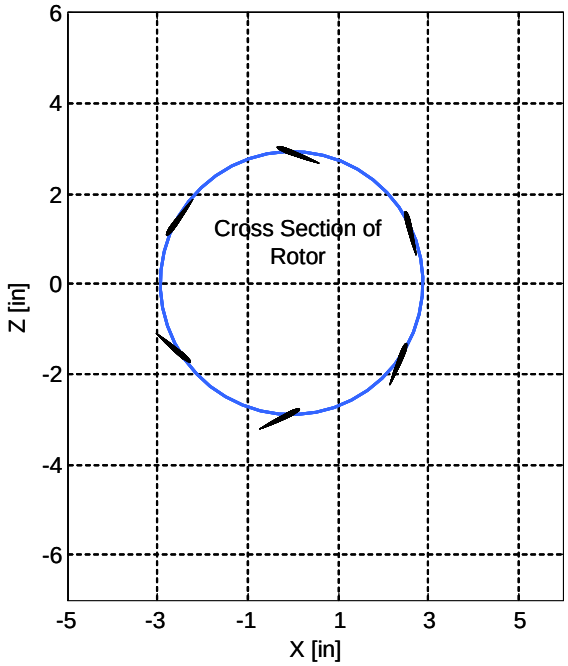

Figure 4.17: Pressure Measurement Coordinate Axis Definition, Flow Cross Section

Chapter 5

Experimental Results and Discussion

5.1 Non-Dimensionalized Coefficients

Non-dimensional parameters have been employed throughout this section in order to simplify and parameterize the results. The rotor thrust coefficient is a function of the swept area of the rotor and the tip speed of the blades:

$$C_T = \frac{T}{\rho(\pi bd)(\Omega R)^2} \tag{5.1}$$

where πbd is the swept area of the blades and is equal to the total area of the actuator disks used in the derivation of the streamtube theory described in Chapter three. Thrust coefficient may sometimes be referred to as C_{F_x} or C_{F_z}, denoting the thrust in the horizontal or vertical direction only. Power coefficient is defined in a similar manner as

$$C_P = \frac{P}{\rho(\pi bd)(\Omega R)^3} \tag{5.2}$$

From the principle of conservation of energy, the power consumed by the rotor can be written as

$$P = T v_u \sin\Psi \tag{5.3}$$

This is the ideal power required by the rotor and neglects any viscous effects on the blades. Rewriting,

$$P_{ideal} = Tv_u \sin\Psi = T\cos\Psi\sqrt{\frac{T}{2\rho A(\cos\Psi)^2}} = \frac{T^{\frac{3}{2}}}{\sqrt{2\rho A}} \tag{5.4}$$

Inflow ratio, λ_h, is equal to

$$\lambda_h = \frac{v_u \cos\Psi}{\Omega R} = \frac{1}{\Omega R}\sqrt{\frac{T}{2\rho A}} = \sqrt{\frac{C_T}{2}} \tag{5.5}$$

Therefore, the ideal power coefficient may be written as

$$C_P = C_T\lambda_h = \frac{C_T^{\frac{3}{2}}}{\sqrt{2}} \tag{5.6}$$

Figure of merit is used as an efficiency factor, defined as

$$FM = \frac{C_T^{\frac{3}{2}}}{\sqrt{2}C_P} \tag{5.7}$$

and is the ratio of ideal (induced) power in hover to actual power required. Another efficiency metric, power loading, will also be used for comparison. Although it is a dimensional quantity, power loading can be helpful in determining the effectiveness of the concept for use on an MAV. Power loading is given as

$$PL = \frac{T}{P} = \frac{\sqrt{DL}}{\sqrt{2\rho}FM} \tag{5.8}$$

Therefore, the best efficiency (in terms of power loading) is occurs when figure of merit is a maximum and disk loading is minimized.

5.2 Thrust

Thrust of the experimental cycloidal rotor was measured across a range of blade pitch angles and rotational speeds to fully characterize its performance. Thrust was measured at average blade pitch angles of 10, 20, 30, and 40°. Maximum tested blade pitch angle was limited to 40° by the constraints of the offset mechanism (Fig. 4.12. In each case, the offset mechanism was positioned such that its movement was limited to the vertical direction ($\Psi = 0$ and 180°), and was situated such that the rotor was thrusting down to preclude the possibility of ground effect influencing the tests. For each case, measurements were recorded at rotational speeds ranging from 0 to 1200 RPM in increments of 200 RPM. Testing at speeds higher than 1200 RPM was limited to prevent damage to the torque cell from transient loads. The rotor was tested in this manner in both a six-bladed as well as a three-bladed configuration.

For each test condition, the rotor was run up to speed and five data points were recorded from each of the two load cells, which were then averaged. The rotor was then stopped, and a zero reading was recorded for each load cell. Measured thrust was the difference between the two values. The sequence was then repeated until ten thrust values were measured for each test condition. Torque and RPM were measured in a similar manner. This system of measurement provided a high level of fidelity in the data.

The vertical force is plotted against rotational speed in Fig. 5.1 for the six-bladed configuration, and in Fig. 5.2 for the three-bladed configuration. Results from the analytical model described in Chapter three are also shown for both cases.

The experimental data agrees well with the predicted values for the three-bladed case. However, in the six-bladed configuration the model significantly over-predicts the experimental results. This discrepancy may be due to interference between the blades in the six-bladed configuration. With six blades, there is approximately three chord lengths before the next blade hits the wake of the previous blade. The flow is still highly unsteady, and may have a profound effect on the impinging blade. It is probable that the assumption made in the analytical model that cascade effects between the blades are negligible is incorrect. Further work in this area may be necessary to accurately predict the loads in this case.

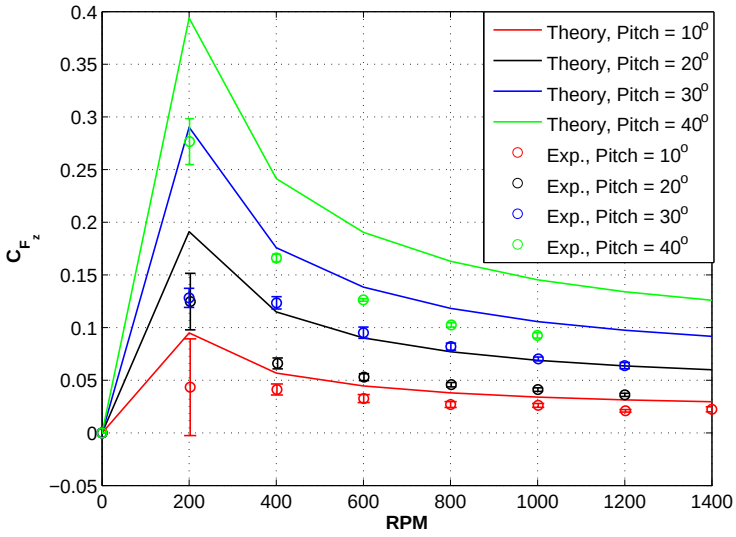

Figure 5.1: Comparison of Theory and Experiment, z-Force vs. RPM, 6 Blades

An important detail to note is the that configuration with six blades does not produce twice the thrust of the three bladed case. The blades on the downstream half of the rotor, from $\Psi = 270°$ to $90°$, see a significant downwash from the upstream blades. This results in a decrease in induced velocity and reduction lift produced by

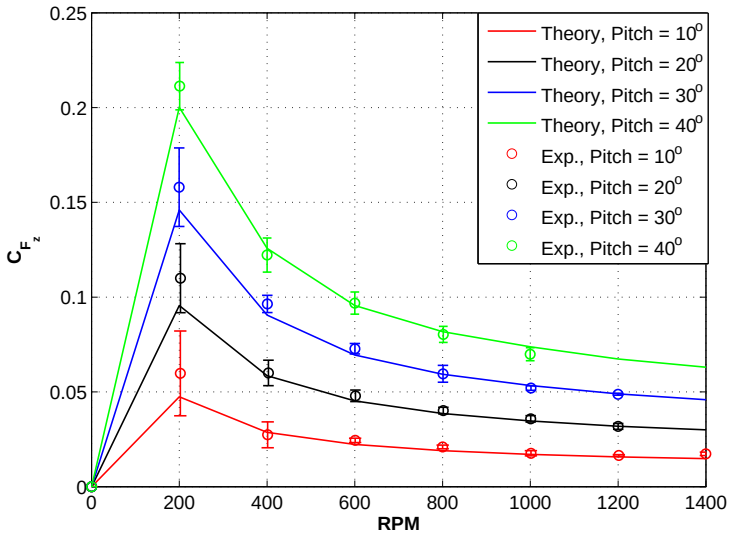

Figure 5.2: Comparison of Theory and Experiment, z-Force vs. RPM, 3 Blades

the downstream blades. Thus, doubling the number of blades should not produce twice the lift. The experimental data bear this out, as the thrust increase for the six-bladed case is only one-third greater than the configuration with three blades.

As blade pitch angle exceeds the static stall angle for the airfoil, there is no drop in thrust, with the implication that the rotor is not experiencing stall in the usual manner. This remains true even as the pitch angle reaches 30° and 40°. There are two effects that may contribute to the unusually high pitch angle that the rotor can achieve without detrimental effects. First, the downwash through the rotor is significant, and this induced inflow would significantly decrease the effective blade angle of attack, particularly at $\Psi = 0°$ and 180°, where pitch angle is greatest.

Another possible contributing factor may be the occurrence of a stall delay phenomenon. As the blade element angle of attack is periodic in nature, separation and stall should occur in a very time-dependent manner. Dynamic stall causes a

delay in flow separation to a higher angle of attack than typically seen in static stall. This has a performance advantage, in that the airfoil is able to achieve higher lift than would be possible in a static situation. However, when separation does occur in this condition, a strong vortex is shed from the leading edge of the airfoil and swept over the blade into the blade wake. The result is a shift in the center of pressure, causing a large nose-down pitching moment on the airfoil and increased torsional loads on the blade [26]. It is not possible to detect the occurrence of dynamic stall in the present setup. Hence, its effects cannot be validated without further experiment.

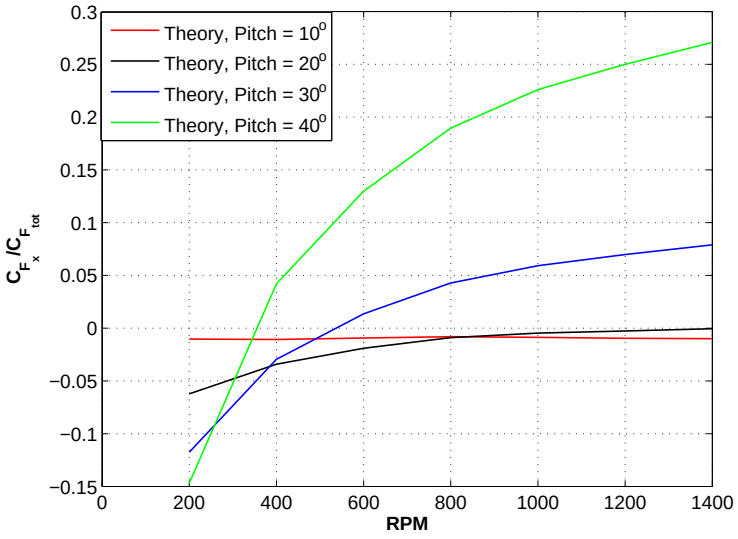

Figure 5.3: Predicted Horizontal Force as a Function of Blade Pitch Angle, 6 Blades

Figs. 5.3 and 5.4 show the horizontal force predictions for the six and three-bladed configurations, respectively, as a percentage of total force,

$$C_T = \sqrt{C_{F_x}^2 + C_{F_z}^2} \tag{5.9}$$

Although the test apparatus did not allow for the measurement of thrust in

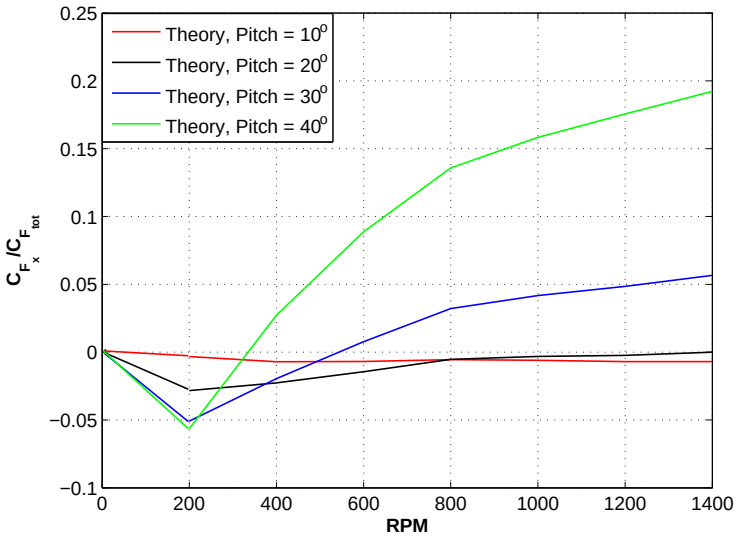

Figure 5.4: Predicted Horizontal Force as a Function of Blade Pitch Angle, 3 Blades

two directions, the validity of these predictions will be carried out later. Note that the horizontal force rises dramatically with blade pitch angle, and at higher blade pitch angles produces greater than 25 percent of the total thrust in the six-bladed case. This large x-force contribution to thrust at high pitch angles is primarily a result of the location of the offset eccentricity, which causes a rotation of the thrust vector around the rotor azimuth.

Referring to Figs. 3.5 and 4.5, the maximum blade pitch angles for the offset mechanism will occur when linkages L_2 and L_3 are parallel. However, the angle, θ_2, at which this takes place will vary depending on the desired pitch angles. Therefore, to simplify data acquisition and maintain consistency in the measurements, the rotor was positioned such that L_2 was always vertical. Thus, from Fig. 5.5, the maximum blade pitch angles do not appear at $\Psi = 0$ and 180°, but at a phase lag approaching 10° with respect to direction of the offset.

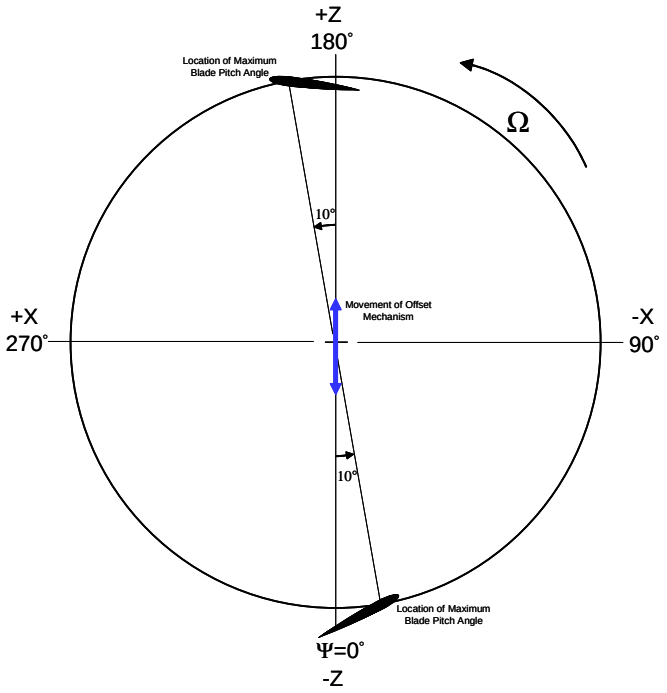

Figure 5.5: Relationship Between Pitch Angle and Offset Mechanism

5.3 Offset Eccentricity

To determine these phase lag, or eccentricity, at which the maximum vertical thrust occurs, a series of experiments were conducted. Eccentricity is defined such that it is equal to zero when the offset for the pitch mechanism occurs at $\Psi = 180°$. This is the position pictured in Fig. 5.5, and the condition in which the thrust measurements shown in Figs. 5.1 and 5.2 were recorded. In this condition, the rotor is thrusting toward the ground, eliminating any possibility of ground effect. Eccentricity is positive when measured in the same direction as rotor rotation. For this series of tests, thrust was measured at blade pitch angles of 0, 10, 20, 30 and 40°. At each pitch angle, the eccentricity, ϕ, was varied from $-50°$ to 50° in 10° increments. Rotational speed was held constant at 800 RPM.

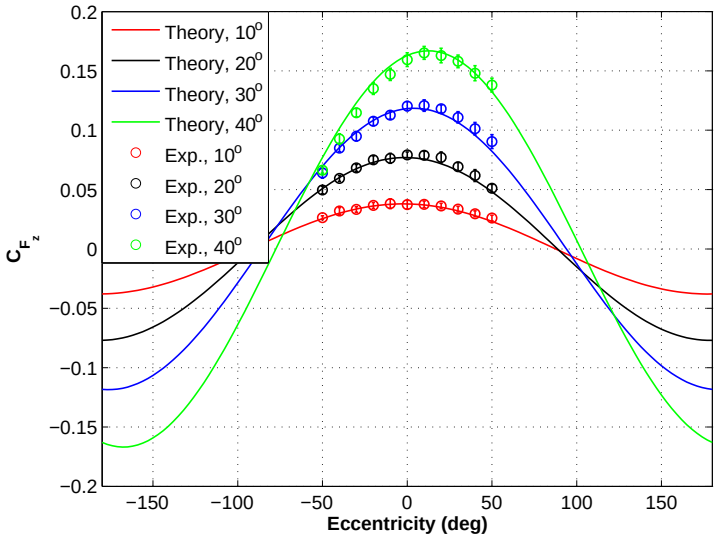

Figure 5.6: Comparison of Theory and Experiment, z-Force vs. Offset Eccentricity, 800 RPM, 3 Blades

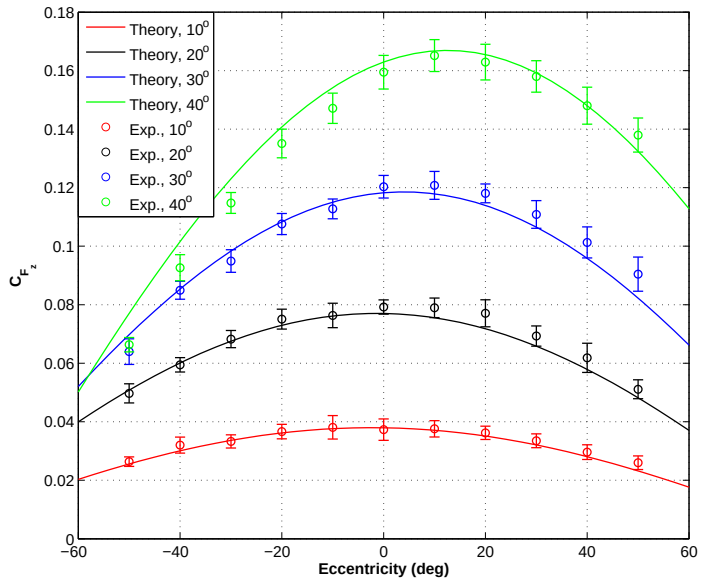

Figure 5.7: z-Force vs. Offset Eccentricity, Expanded View

Fig. 5.6 plots the experimental measurements as well as the predicted values for the eccentricity location. Note that if the eccentricity were 180°, the rotor thrust would be in the opposite direction with the same magnitude. Examining the region that was tested, shown in Fig. 5.7, demonstrates the results agree very well with the predictions. As blade pitch angle is increased, the location of maximum thrust changes. From the model, for pitch angles of 0, 10, and 20°, maximum thrust occurs very close to an eccentricity of zero. However, at 30° pitch angle, maximum thrust occurs at an eccentricity of +9° (counterclockwise in Fig. 5.5), and at 40° it shifts to +15°. As the phase lag between eccentricity and the location of maximum pitch angle is approximately 10°, it is unknown why the position of maximum thrust shift beyond this value. It is possible that the unsteady components of thrust, which are dependent on angular velocity and acceleration of the blade about its quarter chord may have an effect on the maximum thrust location. It is difficult to determine if the same phenomenon occurs in the experimental data, as the small difference in thrust magnitude between 10° and 15° lies within the experimental error. Nevertheless, the experimental results show the same general trend in the data, with the location of maximum thrust occurring forward of the vertical offset at 0°.

5.4 Power

A series of tare tests were performed on the rotor to determine the power consumed by the end plates and the mechanical (friction) losses associated with the mechanism. For this, the blades were removed from the rotor. Power was

calculated by measuring the torque and rotational speed of the rotor and then finding the product of the two ($P = Q\Omega$). The experiments were performed in the same manner as previously mentioned.

The experimental results of the tare tests are shown in Figs. 5.8 and 5.9, which show the mechanical power contributions to the total power consumed by the rotor. For clarity, error bars were not shown on the plots. Mechanical power, found by calculating the difference between total and aerodynamic power measurements, contributes a significant portion of the total power, particularly at lower blade pitch angles. Excessive friction in the rotor components is the source of the large mechanical power component. Note that in each case, mechanical power requirements remain relatively constant for changes in blade pitch angle up to 30°. This is to be expected, as changes in pitch angle should not increase friction of the mechanism. However, at a pitch angle of 40°, mechanical power increases substantially. This may be a result of interference between the linkages and the end plate on the test rotor. At the highest pitch angle setting, the control linkages made slight contact with the arms of the end plate. The problem may have been exacerbated while the rotor was running because the centrifugal forces acting on the blade would have increased the interference.

Figs. 5.10 and 5.11 show the aerodynamic power requirements for the cycloidal rotor for the two cases. Predicted requirements are plotted for comparison. Aerodynamic power was found from the difference of the total power requirements and the mechanical power, determined from the tare tests. In general, the experimental power requirements are slightly higher than the predicted values. This should be

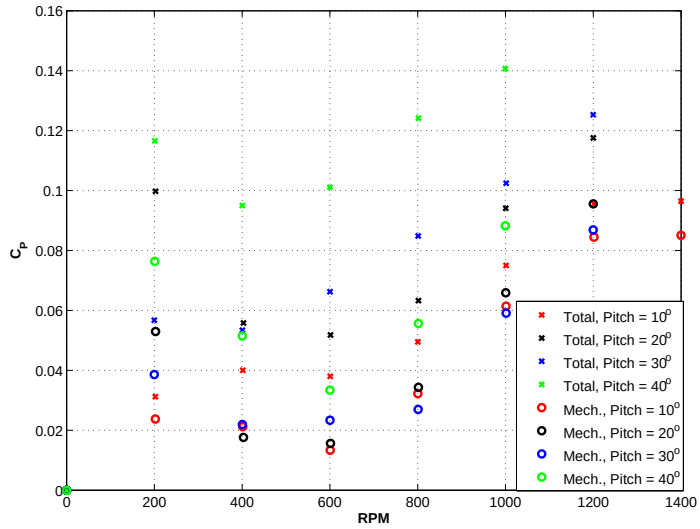

Figure 5.8: Power Breakdown of Cycloidal Rotor, 6 blades

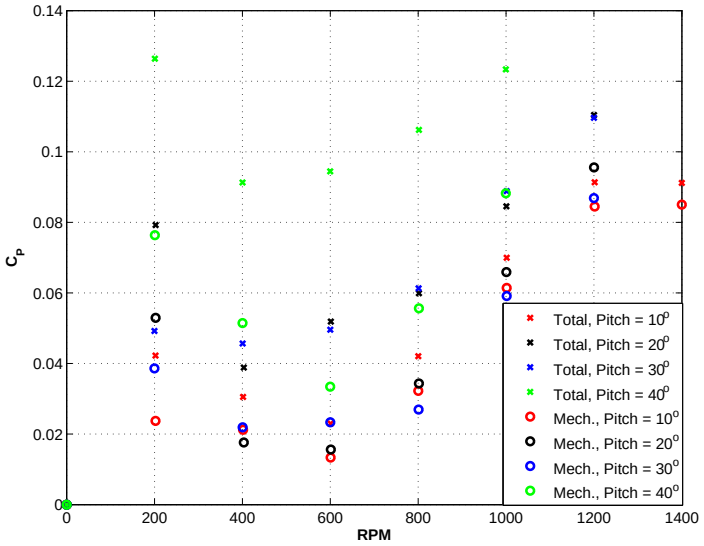

Figure 5.9: Power Breakdown of Cycloidal Rotor, 3 blades

expected, as the analytical values represent the ideal case, i.e., the minimum power required for the blades. This encompasses profile and induced power, as well as the power required to maintain the blade oscillation, which is dependent on the kinetic energy of the vortex wake and the work done by the propulsive force. Furthermore, although the six-bladed case should ideally require twice the power of the three-bladed rotor, the data shows an increase of around 50% for the rotor with six blades. The reasons for this are unknown. However, it may be that wake interference between the blades for the six-bladed configuration decreased the expected power requirements for the rotor, providing a favorable effect.

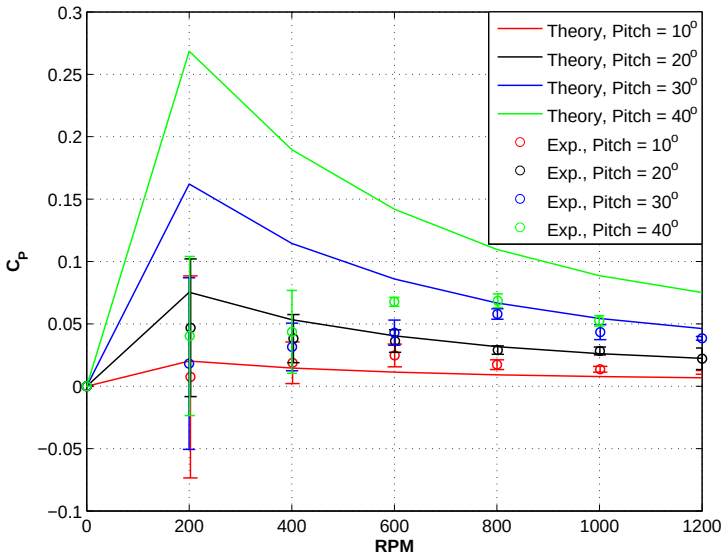

Figure 5.10: Aerodynamic Power as a Function of Blade Pitch Angle, 6 Blades

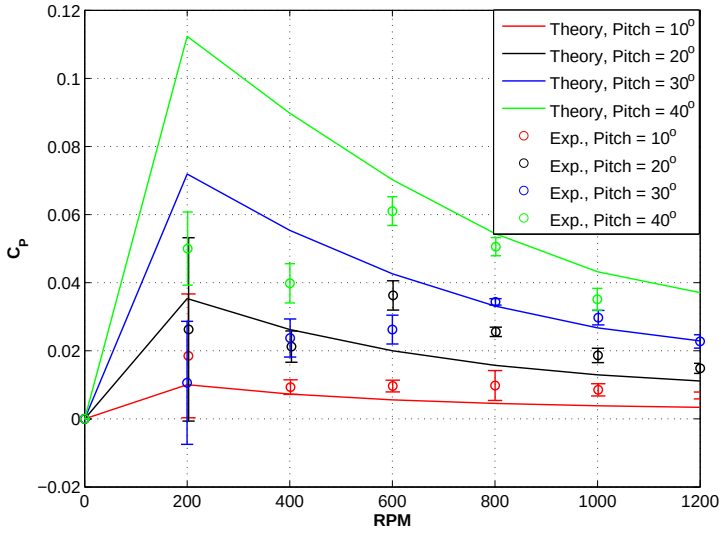

Figure 5.11: Aerodynamic Power as a Function of Blade Pitch Angle, 3 Blades

5.5 Efficiency

To assess the potential of the cycloidal rotor concept, its hovering efficiency was determined and compared to that of a standard rotor of similar dimensions. The relevant parameters of the rotor are provided in Table 5.1. Construction and testing of the rotor was performed by Hein et al. [4] at the University of Maryland. Testing was performed up to blade tip Reynolds numbers of approximately 40,000. In both cases, disk loading was determined using the swept area of the rotor.

Figure 5.12 illustrates the figure of merit for the cycloidal rotor as a function of blade loading coefficient for both the six and three-bladed configurations. Also shown for comparison is the figure of merit of the conventional rotor. Note that at a fixed pitch angle and blade loading coefficient, the three-bladed configuration has a considerably higher figure of merit. Furthermore, at a fixed blade loading coefficient

Parameter	Value
Diameter	6 in.
Chord	0.787 in.
Airfoil Camber	7%
Airfoil Thickness	2.75%

Table 5.1: Parameters of Conventional Rotor

figure of merit decreases as pitch angles increases.

In order to determine the effect of rotational speed on efficiency, Figure 5.13 shows the same data as Figure 5.12 plotted with lines of constant RPM. The cycloidal rotor experiences much higher blade loading coefficients than the conventional rotor, a result of the much lower rotational velocities at which it is run. Moreover, the conventional rotor reaches its peak figure of merit at a very low blade loading. The cycloidal rotor, on the other hand, must have a much higher blade loading to achieve a comparable figure of merit. In addition, although the maximum figure of merit of the two rotors are similar, the cycloidal rotor can only achieve it at very low rotational speeds. This places severe restrictions on thrust output and limits the usefulness of the cycloidal concept.

Figs. 5.14 and 5.15 show the experimental and analytical efficiency ratios for the two cases plotted against disk loading. Again, error bars are omitted for clarity. As mentioned earlier, disk loading is determined from the swept area of the rotor, equivalent to the sum of the area of the actuator disks used in developing the streamtube theory in Chapter three. Predicted values of power loading asymptote

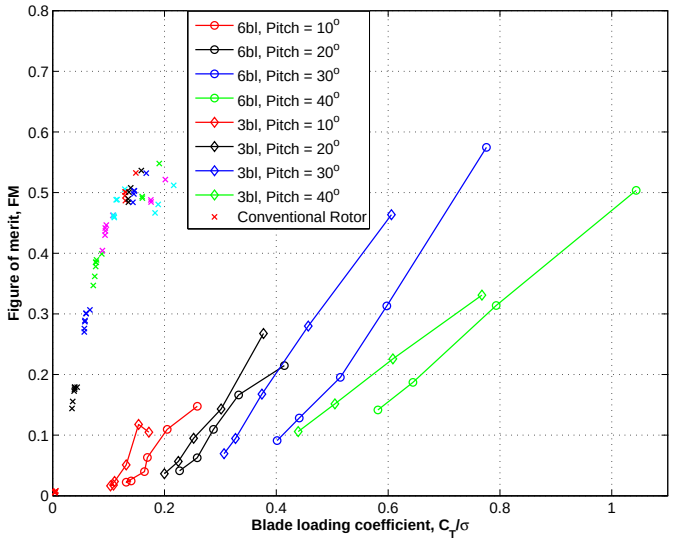

Figure 5.12: Effect of Blade Pitch Angle on Figure of Merit

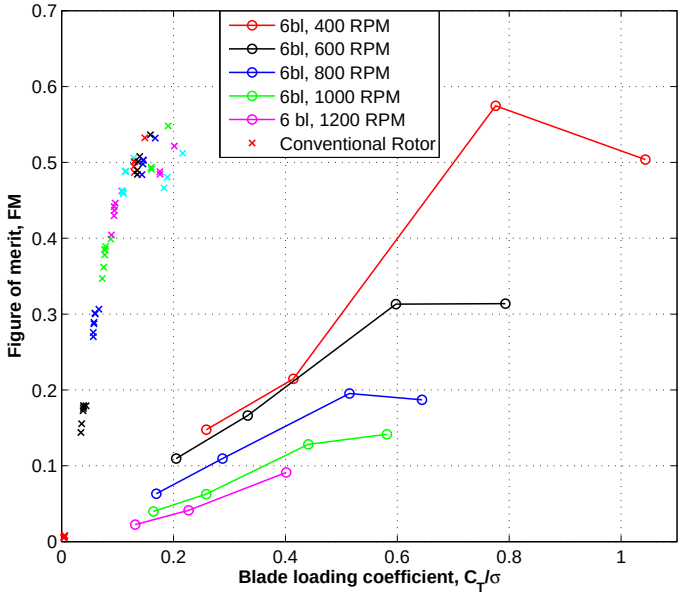

Figure 5.13: Effect of RPM on Figure of Merit

near 0.2 Newtons per Watt (approximately 33.5 lb/hp). The experimental power loadings, however, decrease much sooner than predictions and do not correlate well. Higher pitch angles achieve greater power loadings at a given disk loading as well, indicating it may be beneficial and efficient to run the cycloidal rotor at large pitch angles.

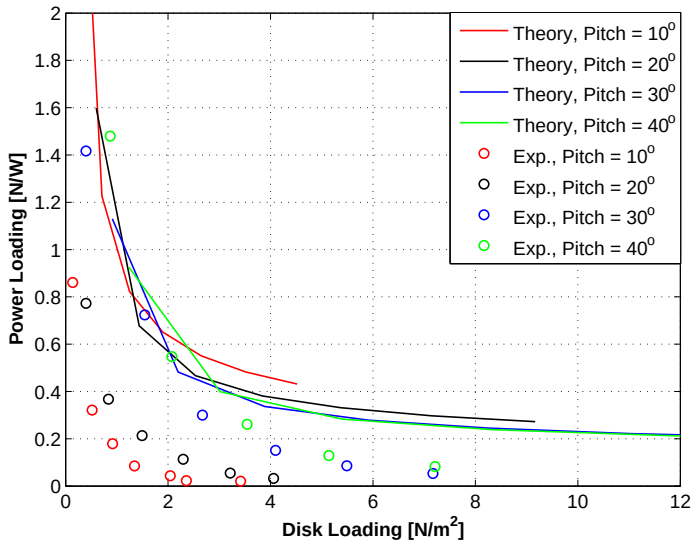

Figure 5.14: Power Loading vs. Disk Loading for 6 blades

Fig. 5.16 compares the power loading of the six-bladed cycloidal with the conventional rotors mentioned earlier. The multiple data sets for the conventional rotor correspond to different collective settings, with power loading increasing with collective. Note that at a given disk loading the conventional rotor achieves a much greater power loading than the cycloidal rotor. The setup of the conventional rotor allowed much higher rotational speeds to be reached compared to the cycloidal rotor, corresponding to higher disk loadings. Although it appears that power loading of the cycloidal rotor will continue to decrease with further increases in disk loading,

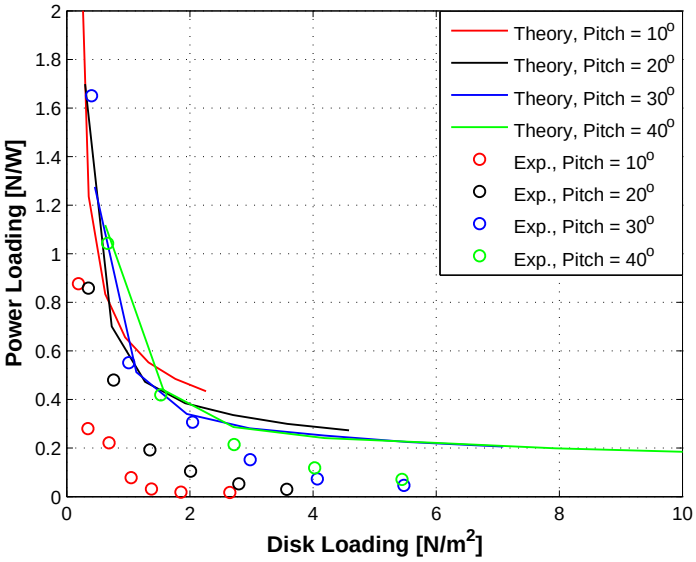

Figure 5.15: Power Loading vs. Disk Loading for 3 blades

additional testing is needed to corroborate this.

5.6 Pressure Measurements

A series of experiments were conducted to obtain an outline of the flow surrounding a cycloidal rotor. Although flow visualization was considered, it was determined that, at this time, quantitative measurements would be of more use. Therefore, the pressure measurement technique described in Chapter 4 was implemented.

The test setup for the experiment provided a high degree of precision for taking measurements. Pressure measurements were recorded at location of $\frac{1}{2}$, 3, 6, and 9 inches below the rotor, as previously illustrated in Fig. 4.16. Rotational speed was held constant at 1100 RPM. The area over which measurements were taken was sufficient to capture the majority of the downwash. In unsteady flow such as that

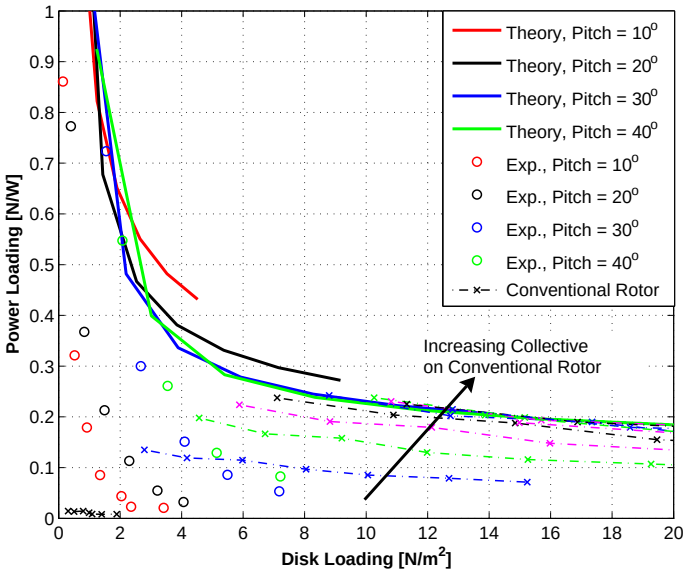

Figure 5.16: Comparison of Cycloidal Rotor with Conventional Rotor

experienced by the cycloidal rotor, the pressure drop is out of phase with the flow rate. An unsteady correction term may be used to correct for the phase difference. The results shown for this series of experiments, however, are the average of a set of pressure measurements and are thus the sum of the steady inflow velocities and the average of the unsteady inflow velocities.

The first set of measurements were taken with the first generation rotor fastened in the cantilever test stand. Fig. 5.17 illustrates the downwash at three inches ($\frac{1}{2}$ rotor diameter) below the model rotor. The outline shows the position of the rotor, rotating clockwise (toward the left side of the page). The downwash at nine inches below the rotor is shown in Fig. 5.18. Note that induced velocities remain relatively high. Moreover, the high velocity regions of induced velocity have shifted toward the fixed end of the setup. Subsequent measurements revealed that the rotor

experienced a loss of downwash over the outer portion of the rotor. It was surmised that vibrations in the rotor, in large part because of the cantilever setup, were the source of this effect.

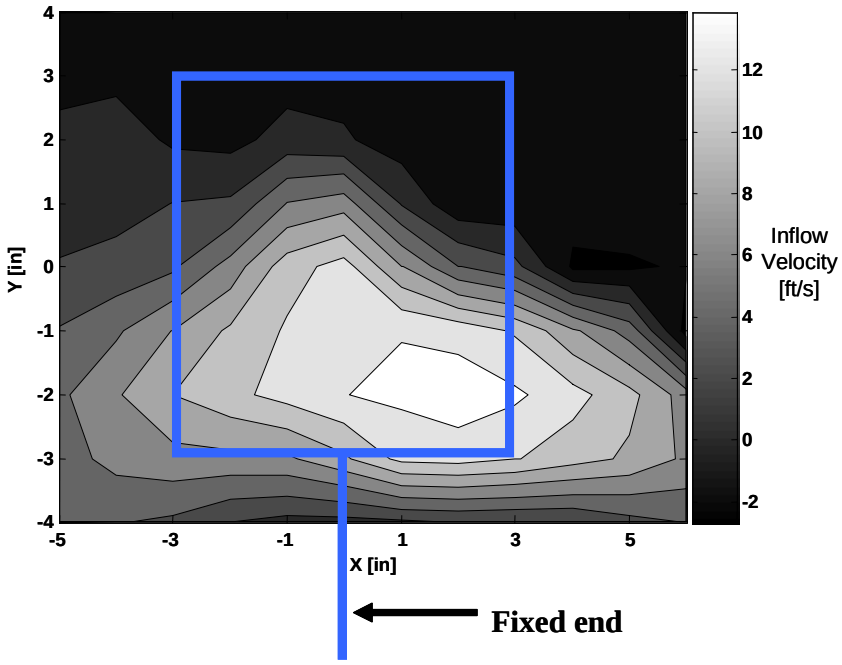

Figure 5.17: Downwash Three Inches Below Cycloidal Rotor, Cantilevered, 1100 RPM

The rotor was then tested with both ends clamped in an attempt to correct the problem. Fig. 5.19 demonstrates the results of the change. The flow is symmetric in this case, as expected. Measurements for each case were then repeated with the new setup. By documenting the change in location of the maximum flow velocities at different positions below the rotor, it was determined that the outflow was directed approximately 15° from the vertical axis of the rotor, at about $\Psi = 15°$. This is an average value, as results between measurements varied between 10° and 20°.

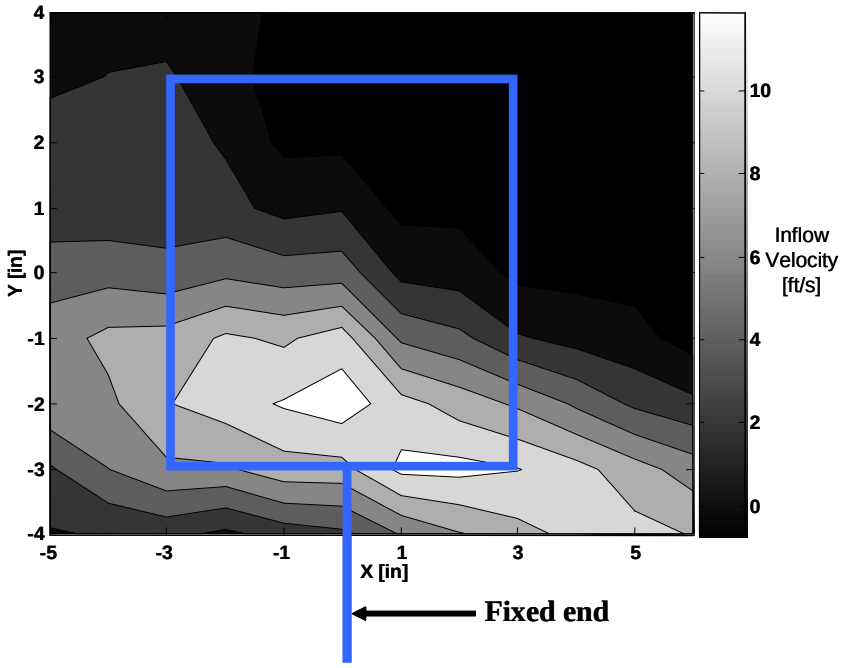

Figure 5.18: Downwash Nine Inches Below Cycloidal Rotor, Cantilevered, 1100 RPM

Maximum measured inflow velocities approached 14 ft/s substantially higher than predicted values of 8.5 ft/s. A more rigorous application of streamtube theory is recommended for better correlation with predictions.

A cross-section of the flow was then measured, taken at mid-span of the rotor. Measurements inside the rotor were not possible. The results are shown in Fig. 5.20. The induced airflow through the top of the rotor is reasonably uniform; this is expected, as it should flow into the rotor in a direction normal to the circular path of the blades. Note that the inflow is greatest in the lower left quadrant of the rotor, and are then swept in the direction of rotation to the right. It is assumed that the refraction of the airflow is caused by the downwash of the upstream blades affecting the downstream blades in the lower right quadrant. This downwash would have

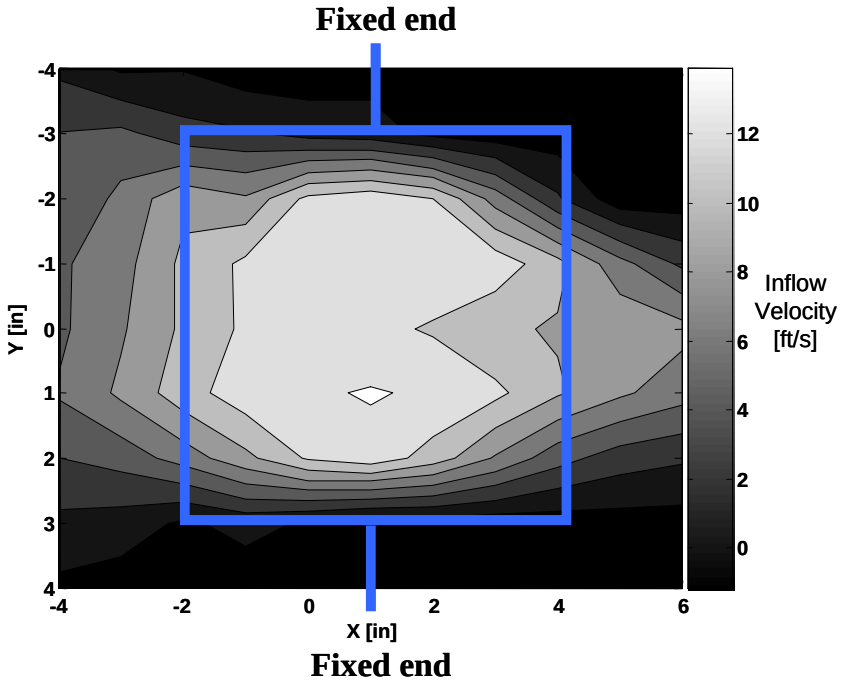

Figure 5.19: Downwash Three Inches Below Cycloidal Rotor, Clamped Ends, 1100 RPM

the effect of increasing the inflow velocity on the downstream blades, deflecting the airflow. From the figure, it appears that the slipstream expands as it exits the rotor. This contradicts the flow model assumptions made in Chapter three. However, the flow cross-section is too small to make that assertion with any confidence, and further testing of the wake structure below the rotor, either through flow visualization or improved pressure measurements, is necessary to substantiate that claim.

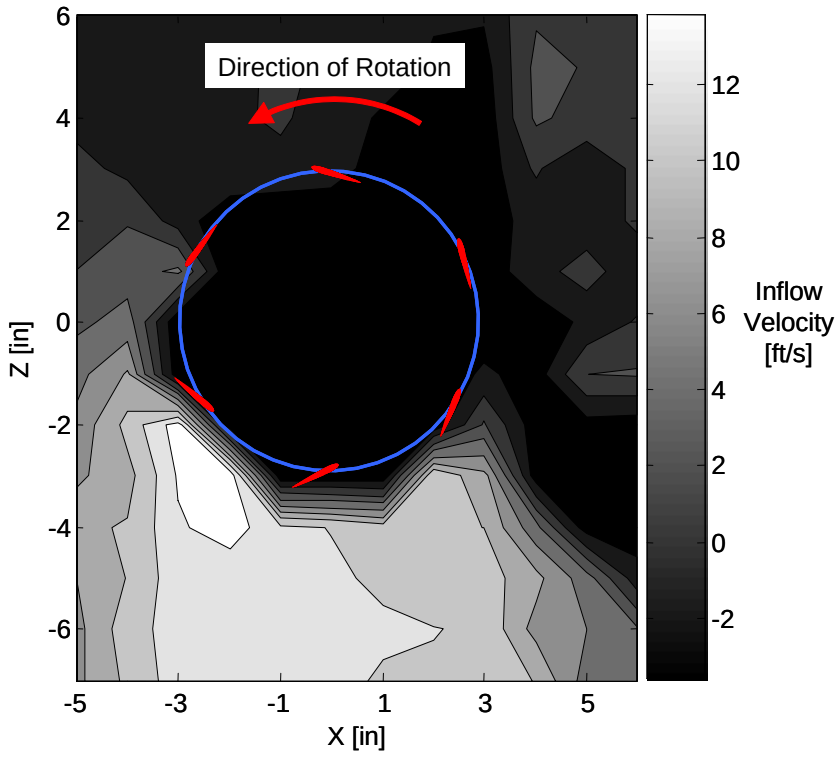

Figure 5.20: Cross Section of Flow Through Cycloidal Rotor, 1100 RPM

Chapter 6

Conceptual Design of Cyclo-MAV

A paper study was conducted to determine, based on the experimental results presented in Chapter 5, the feasibility of implementing the cycloidal propulsion concept on a micro air vehicle. A vehicle, using two cycloidal rotors of the same dimensions as tested in the current work, was designed using CATIA V5 CAD software [47].

6.1 Design Elements

The complete vehicle design is pictured in Fig. 6.1. A three-bladed rotor was chosen for the design, as this configuration displayed greater efficiency ratios than a six-bladed design. Furthermore, there was no evidence during testing of wake interference with the three bladed design.

Blades should be constructed in a manner similar to the earlier approach. However, a carbon rod, located at the quarter-chord, will stiffen the blade against the significant transverse centrifugal blade loading inherent to the cycloidal design if it is is inserted into the foam before the curing process. Furthermore, as the carbon rod will be coincident with the pitch bearing, it can act as the pivot point for the blade pitching motion (Fig. 6.2).

Blades will be attached at one end to a three-arm frame fabricated from carbon

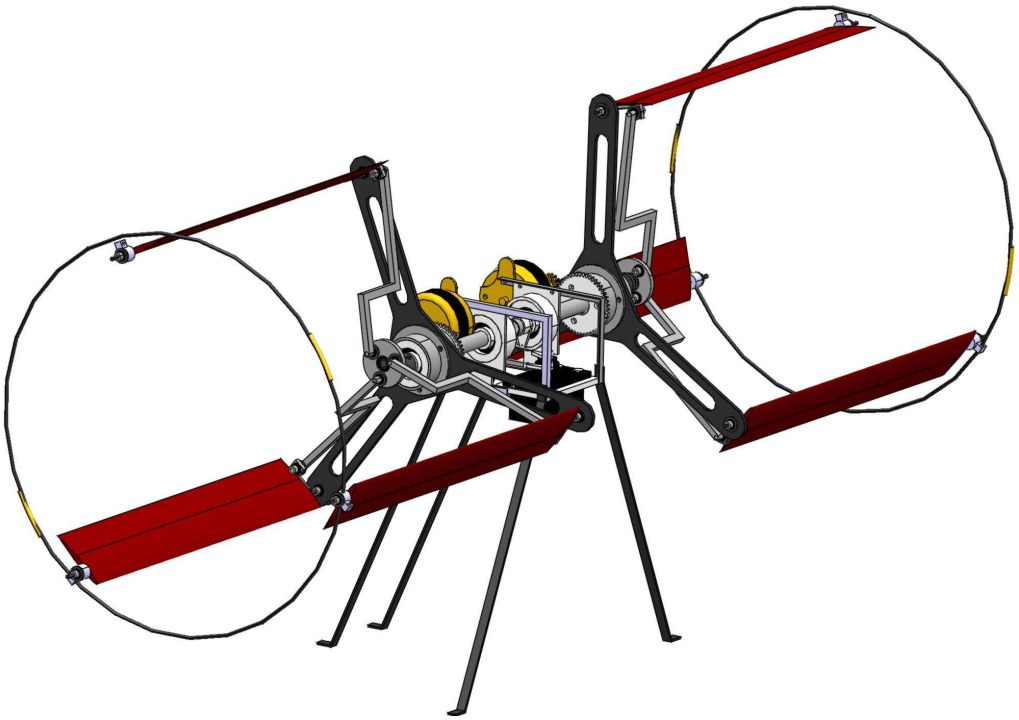

Figure 6.1: Conceptual Cycloidal Rotor MAV

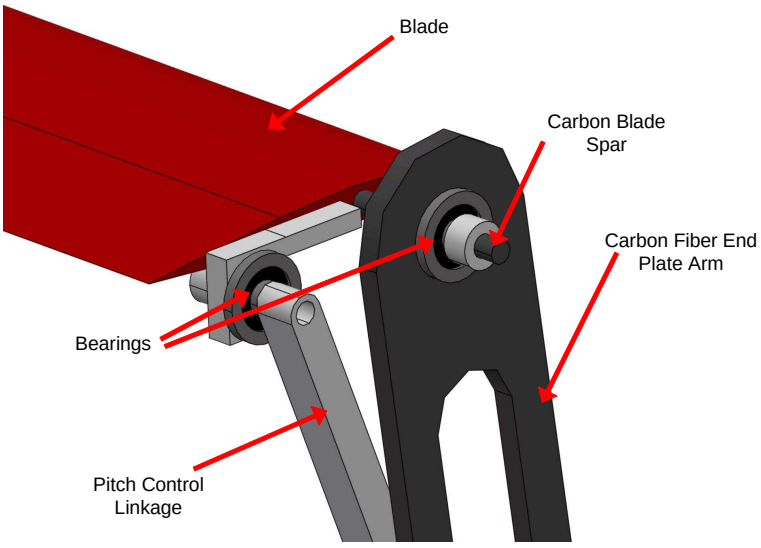

Figure 6.2: Blade Pivot Arrangement

fiber; at the other end, the blades will be held together by a carbon ring. This design should eliminate a considerable amount of weight over the current configuration, while still limiting the bending moment of the blade to acceptable levels.

Rotors will utilize a fixed pitch offset mechanism to achieve the required change in blade pitch angle (Fig. 6.3). Although a variable pitch mechanism similar to that used on the experimental rotor was considered, a fixed pitch design can be made much lighter. The mechanism should be set such that the maximum pitch angle of the blades is $\pm 30°$, as the experimental results showed an increase in figure of merit at this setting (Figs. 5.12 and 5.13).

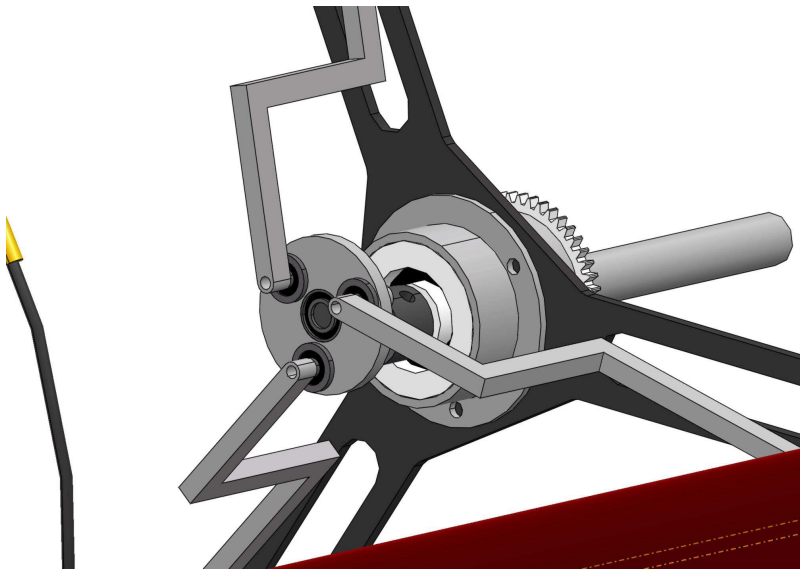

Figure 6.3: Fixed Pitch Offset Mechanism

Directional control of the vehicle shall be achieved by rotating the driveshaft of each rotor, which will change the azimuthal location of the offset mechanism. The rotor driveshafts, both coincident with shaft bearings, will allow the rotors to rotate freely in any direction. The control mechanism will consist of two small servos,

shown in Fig. 6.4, mounted between the rotors. Actuation of the servos, which will be connected to the driveshaft through a linkage arrangement, would rotate the entire rotor, changing the direction of thrust. This use of mechanical actuation for directional control should provide the vehicle with exceptional maneuverability and handling characteristics.

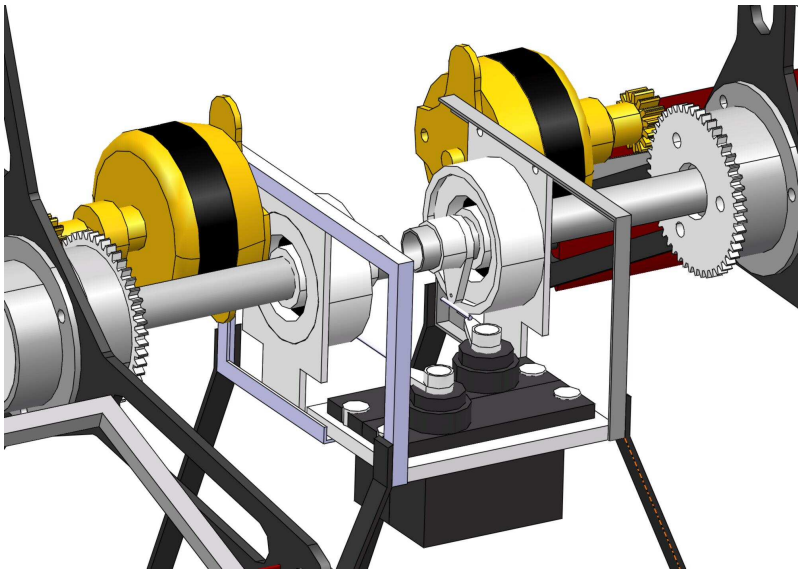

Figure 6.4: Directional Control of Thrust Vectors

The electronic package needed for vehicle control will include a receiver, lithium-polymer battery, and two speed controls, necessary for management of the two brushless motors. Although not shown on the vehicle, these components could easily be positioned below and aft of the rotor axes such that their weight would provide the necessary torque compensation for the motors, allowing the reaction couple between thrust and vehicle weight to reach static stability. This setup would eliminate the need for an additional device for torque compensation and its accompanying weight penalty. A weight breakdown of the vehicle components is provided in Table

6.1.

Component	**Weight (g)**	**% Total**
Electronics (Receiver, speed controls)	27	10.9
Li-Po Battery (1500 mAh)	50	20.3
Motors (brushless DC)	47.8	19.3
Servos	12.5	5.1
Rotors (Combined)	91.3	37.0
Structure (Frame, landing gear, mounting hardware)	18.5	7.49
Total	**247.1**	**100**

Table 6.1: Component Breakdown of Cyclo-MAV

Table 6.2 list the weight breakdown of a more conventional MAV. This vehicle, shown in Fig. 6.5, was designed and constructed at the University of Maryland by Sirohi et al. [48]. From the weight breakdowns for the two vehicles, electronics and the battery contribute a large percentage of the vehicle weight. As technology in these areas improves their weight contributions will decrease. The two rotors on the cyclo-MAV contribute 37% of the total weight. Note that this also includes the blade pitch mechanism and rotor control, equivalent to the swashplate assembly on a conventional helicopter. Conversely, the combined rotor and swashplate assembly on the conventional MAV contribute just 11% of the vehicle weight. The high rotor weight on the cyclo-MAV may make vehicle control more difficult, as inertial loads will significantly increase. Furthermore, with the cycloidal configuration, much of the rotor weight is placed at the outer diameter of the rotor, akin to adding

tip weights to a conventional rotor. Careful balancing of component masses, then, is critical for minimizing vibrations and achieving acceptable handling qualities. Another point of note with the cyclo-MAV is its significant reduction in airframe structure, which serves to retain the motors, driveshaft, servos, and electronics components. As a percentage of total vehicle weight, the structure of the cyclo-MAV is only one-fourth that of the conventional rotor MAV.

Component	**Weight (g)**	**% Total**
Electronics and servos	38	15.9
Li-Po Battery (1500 mAh)	53.3	22.2
Motor (brushless DC)	52.7	22.0
Rotor system	18.3	7.6
Swashplate	8.1	3.4
Structure	69.2	28.9
Total	**239.6**	**100**

Table 6.2: Component Breakdown of Conventional MAV

Based on the results from the paper study, the rotors on the cyclo-MAV will require a minimum rotational speed of 1650 RPM to achieve the necessary thrust of 125 grams per rotor. A speed of 1875 RPM should provide enough additional thrust for propulsion and control. Although the experimental rotor was tested at slightly lower speeds, it was limited primarily to prevent damage to the test stand. The improvements introduced in the cyclo-MAV and its lower weight should also prove beneficial in reducing vibrations.

Figure 6.5: Conventional Rotary Wing MAV

Based on the experimental work and the study described above, a micro air vehicle utilizing cycloidal propulsion is feasible.

Chapter 7

Conclusions and Future Work

7.1 Conclusions

A small-scale cycloidal rotor was designed and constructed to determine if the system was practical for use on a micro air vehicle. Its performance was then measured experimentally and compared to predictions. A first generation cycloidal rotor, constructed previously, was tested as a first attempt at determining its characteristics. However, problems with the design precluded any significant results from the tests. Vibrations with the rotor and the limitations of the test stand, in particular, proved challenging. A second generation rotor using the cycloidal blade system was constructed to resolve the issues with the first rotor. The new design permitted the pitch angle of the blades to be varied from 0° to 40°. A more rigid design, coupled with careful balancing of components, decreased vibrations by an order of magnitude. A new test stand was also constructed that allowed thrust, torque, and rotational speed to be measured.

A theory was developed in an attempt to predict the performance of the test rotor. The analysis uses a streamtube model from wind turbine theory in conjunction with the superposition of the indicial aerodynamic response to a step change in angle of attack, found by a formulation of the aerodynamic force and moment equations utilizing the Wagner function.

An investigation of the flow field around the model rotor proved useful in obtaining a view of the rotor downwash. It was found that the outflow was directed approximately 15° from the vertical, after passing the downside blades of the rotor.

Using the second generation rotor, thrust and power were determined as a function of rotational speed and blade pitch angle. Thrust increased with the square of rotational speed, while power increased to the cube of RPM. No reduction in thrust was measured as blade pitch angle was increased from 0° to 40°, indicating that dynamic stall may play a role in the operation of the cycloidal blade system. Tests were conducted on both a six-bladed rotor and a three-bladed rotor. Although the six-bladed case produced greater thrust, the increase was not as great as expected, and it is probable that there may have been wake interference between the blades in that case. The results for the three-bladed case, however, compared well with predictions. Further testing on the effects of the phase angle of eccentricity on the thrust direction determined that vertical force reached a maximum at a phase lag around 15°, close to the predicted values.

By examining the figure of merit of the cycloidal rotor, it was found that operation at lower rotational speeds is desirable to maximize efficiency. Greater pitch angles are necessary to achieve high figures of merit. The efficiency of the cycloidal blade system was also compared with that of a conventional rotor of similar scale. While it is possible to achieve similar figures of merit with the cycloidal rotor, blade loadings are significantly greater. Furthermore, high figures of merit with the cycloidal rotor were achieved only at low rotational speeds. This limits the utility of the concept because at those speeds thrust output is very low.

Power loading for the cycloidal rotor was determined and compared to that of the conventional rotor. At a fixed disk loading, the power loading of the cycloidal rotor was significantly lower. Power loading increased as pitch angle of the blades was increased.

A weight analysis was conducted to determine if the increased weight of the cycloidal blade system would prevent its use on a micro air vehicle. An MAV utilizing cycloidal rotors was modeled in CATIA and optimized for low weight. The completed vehicle, including electronics and battery, weighed approximately 250 grams. Based on predictions, the rotors must rotate at 1650 RPM for the vehicle to produce sufficient thrust. A weight breakdown of vehicle, compared with a rotary-wing MAV of the same size, showed that the rotors on the cyclo-MAV contributed a much larger percentage to the vehicle weight than did the conventional rotor MAV. This has a potentially strong impact on the stability handling characteristics of the vehicle.

From the present work, it appears that while the cycloidal blade system is a viable configuration for a micro air vehicle, it may not be an efficient system. With proper design, the system can produce the necessary lift required for the vehicle. However, to produce the necessary thrust required for such a vehicle, the rotor must be run at speeds where it is much less efficient than a conventional rotor. The complexity and number of parts of the design are also causes for consideration. The large percentage of the vehicle weight concentrated in the rotors may make vehicle control more difficult as well. These drawbacks notwithstanding, the cycloidal configuration may be suited for a particular function if one is willing to accept the

weaknesses of the design. Its implementation on marine systems has shown the tremendous maneuverability of the cycloidal system. If an application warrants such maneuverability, there may be a justification for developing a cyclo-MAV.

7.2 Future Work

To investigate its possible benefits over a conventional MAV configuration, a cycloidal rotor MAV must be constructed and tested. It must be determined whether the potential benefits of the design carry over to a viable vehicle. Control algorithms for hovering and steady, level flight must be developed for the design.

Optimization of the design must be conducted to maximize its usefulness. Ref. [29] has shown that the NACA 0012 is extremely sensitive to variations in Reynolds number or turbulence, and is unsuitable for Reynolds numbers less than 50,000. Based on Ref. [4], a flat plate blade with sharpened leading edge may prove to be a better airfoil than the NACA 0010 used on the test rotor in the present work. Careful design of such blades is necessary, though, to ensure their strength and stiffness are able to withstand the high transverse centrifugal loadings without large deformation taking place. Blades with larger chords would increase Reynolds number and may prove beneficial, although any benefits may be offset by the increase in solidity of the rotor, which decreases performance. It may also be worthwhile testing a four bladed configuration of the design.

Computational fluid dynamics (CFD) analysis would not only be useful in validating existing experimental and theoretical results, but would provide an excellent

means of visualizing and understanding the flow conditions around the rotor.

Improvements must also be carried out on the cycloidal rotor analysis. Although cascade aerodynamics should not have had a significant effect on the model, it was apparent from the data that some interactions between blades and blade wakes were taking place in the six-bladed configuration. Furthermore, [12] has demonstrated a virtual camber effect, in which the rotation of the rotor causes the blade to behave like a cambered airfoil. This may have a significant impact on aerodynamic characteristics, particularly if large chord blades are utilized, and it may be beneficial to investigate this further.

Finally, it must be remembered that the mechanism currently used to provide periodic changes in blade pitch is ideal only for hovering conditions. An investigation of the blade motions at various forward flight speeds, and the mechanisms needed for producing them, must be carried out. Individual blade control, while probably the optimal configuration, would be difficult to implement on a small vehicle and would incur a significant weight penalty. A series of cams, each optimized for different flight speeds may prove to be a workable solution. The efficiency and handling of a cycloidal rotor micro air vehicle must then be determined through systematic experiments.

[1] McMichael, J. and Francis, M., "Micro Air Vehicles - Toward a New Dimension in Flight," http://www.darpa.mil/tto/MAV/mav_auvsi.html, August 1997.

[2] Huber, A., "Death by a Thousand Cuts: Micro-Air Vehicles (MAV) in the Service of Air Force Missions," *Research Report for the Air War College*, April 2001.

[3] Bohorquez, F. and Pines, D., "Rotor and Airfoil Design for Efficient Rotary Wing Micro Air Vehicles," 61^{st} *Annual American Helicopter Society Forum*, Grapevine, TX, June 2005.

[4] Hein, B. and Chopra, I., "Hover Performance of Micro Air Vehicles: Rotors at Low Re," *American Helicopter Society International Specialists' Meeting on Unmanned Rotorcraft*, Chandler, AZ, January 2005.

[5] Everson, D., Samuel, P., and Pines, D., "Determination of Rotary Wing MAV Stability Derivatives in Hover using a Forced Oscillation Test Stand," 61^{st} *Annual American Helicopter Society Forum*, Grapevine, TX, June 2005.

[6] Conroy, J., Samuel, P., and Pines, D., "The Evaluation of Optic Flow Data Using a Wireless Telemetry System for Micro Air Vehicle Applications," *American Helicopter Society International Specialists' Meeting on Unmanned Rotorcraft*, Chandler, AZ, January 2005.

[7] Stuerzl, W. and Srinivasan, M., "Omnidirectional Vision with Frontal Stereo," *Proceedings of* 27^{th} *Annual Meeting of the German Association for Pattern Recognition*, 2005.

[8] AeroVironment Inc., http://www.aerovironment.com, Location - Monrovia, CA, 2005.

[9] Lockheed Martin, http://www.lockheedmartin.com, Location - Bethesda, MD, 2005.

[10] Seiko Epson Corporation, http://www.epson.co.jp/e/, Location - Nagano, Japan, 2005.

[11] Singh, B., Ramasamy, M., Chopra, I., and Leishman, J., "Experimental Studies on Insect-Based Flapping Wings for Micro Hovering Air Vehicles," 46^{th} *Annual AIAA uctural Dynamics and Materials Conference*, Austin, TX, April 2005.

[12] Kim, S., Yun, C., Kim, D., Yoon, Y., and Park, I., "Design and Performance Tests of Cycloidal Propulsion Systems," 44^{th} *AIAA/ASME/ASCE/AHS Structures, Structural Dynamics, and Materials Conference*, April 2003.

[13] Nagler, B., "Patent number 280849," November 1926.

[14] Kirsten, F. K., "Cycloidal Propulsion Applied to Aircraft," *Transactions of the American society of Mechanical Engineers*, Vol. 50, No. AER-50-12, 1928, pp. 25–47.

[15] Wheatley, J., "Simplified Aerodynamic Analysis of the Cyclogiro Rotating-Wing System," Tech. Rep. 467, National Advisory Committee for Aeronautics, August 1933.

[16] Wheatley, J. and Windler, R., "Wind Tunnel Tests of a Cyclogiro Rotor," Tech. Rep. 528, National Advisory Committee for Aeronautics, May 1935.

[17] McNabb, M., *Development of a Cycloidal Propulsion Computer Model and Comparison with Experiment*, Master's thesis, Mississippi State University, December 2001.

[18] Gibbens, R. P., Boschma, J., and Sullivan, C., "Construction and Testing of a New Aircraft Cycloidal Propeller," *American Institute of Aeronautics and Astronautics*, 1999.

[19] Gibbens, R., "Improvements in Airship Control Using Vertical Axis Propellers," *AIAA* 3^{rd} *Annual Aviation Technology, Integration, and Operations Tech*, November 2003.

[20] Onda, M., Matsuuchi, K., Ohtsuka, N., and Kimura, Y., "Cycloidal Propeller and its Application to Advanced LTA Vehicles," *AIAA* 3^{rd} *Annual Aviation Technology, Integration, and Operations Tech*, November 2003.

[21] Kim, S., Yun, C., Lee, H., Jung, J., Hwang, I., and Park, I., "Design of a New VTOL UAV, Cyclocopter," 60^{th} *American Helicopter Society Forum*, June 2004.

[22] Belloli, A., "*Investigation of a Cycloidal Rotor for Micro Air Vehicles*," Undergraduate Report, University of Maryland, November 2003.

[23] Paraschivoiu, I., Desy, P., and Masson, C., "Aerodynamics of Small-scale Vertical-Axis Wind Turbines," 20^{th} *Intersociety Energy Conversion Engineering Conference*, Miami, FL, August 1985.

[24] Paraschivoiu, I., Fraunie, P., and Beguier, C., "Streamtube Expansion Effects on the Darrieus Wind Turbine," *Journal of Propulsion and Power*, Vol. 1, 1985, pp. 150–155.

[25] Masson, C., "Dynamic and Viscous Effects on the Vertical-Axis Wind Turbine," 26^{th} *AIAA Aerospace Sciences Meeting & Exhibit*, Reno, NV, January 1988.

[26] Leishman, J. G., *Principles of Helicopter Aerodynamics*, Cambridge University Press, New York, NY, 2000.

[27] Bisplinghoff, R., Ashley, H., and Halfman, R., *Aeroelasticity*, Addison-Wesley Publishing Company Inc., Cambridge, MA, 1955.

[28] Beddoes, T., "Practical Computation of Unsteady Lift," *Vertica*, Vol. 8, No. 1, 1984, pp. 55–71.

[29] Laitone, E., "Wind Tunnel Test of Wings at Reynolds Numbers Below 70,000," *Experiments in Fluids*, Vol. 23, 1997, pp. 405–409.

[30] Laitone, E., "Aerodynamic Lift at Reynolds Numbers Below $7x10^4$," *AIAA Journal*, Vol. 34, No. 9, September 1996.

[31] Harrisberger, L., *Mechanization of Motion*, John Wiley & Sons, Inc., New York, NY, 1961.

[32] Hill, P. and Peterson, C., *Mechanics and Thermodynamics of Propulsion*, Addison-Wesley Publishing Co., New York, NY, 1992.

[33] Gostelow, J. P., *Cascade Aerodynamics*, Pergamon Press, New York, NY, 1984.

[34] Horlock, J., *Axial Flow Compressors: Fluid Mechanics and Thermodynamics*, Buttersworths Publications Limited, Hertfordshire, UK, 1958.

[35] Johnsen, I. and Bullock, R., editors, *Aerodynamic Design of Axial-Flow Compressors*, National Aeronautics and Space Administration, Washington, D.C., 1965.

[36] Strickland, J., "A Review of Aerodynamic Analysis Methods for Vertical-Axis Wind Turbine," *Fifth ASME wind Energy Symposium, presented at the Ninth Annual Energy Sources Technology Conference*, February 1986, pp. 7–17.

[37] Leclerc, C., "Why use natural laminar flow airfoils in vertical axis wind turbine applications?" 26^{th} *AIAA Aerospace Sciences Meeting & Exhibit*, Reno, NV, January 1997.

[38] Garrick, I., "Propulsion of a Flapping and Oscillating Airfoil," Tech. Rep. 567, National Advisory Committee for Aeronautics, 1937.

[39] AeroModel, http://www.aero-model.com, Tempe, AZ, 2005.

[40] National Instruments, http://www.ni.com, Austin, TX, 2005.

[41] MathWorks, http://www.mathworks.com, Natick, MA, 2005.

[42] Vishay Measurements Group, http://www.vishay.com, Malvern, PA, 2005.

[43] Transducer Techniques Inc., http://www.transducertechniques.com, Location - Temecula, CA, 2005.

[44] United Sensor Corporation, http://www.unitedsensorcorp.com, Location - Amherst, NH, 2005.

[45] Setra Systems Inc., http://www.setra.com, Location - Boxborough, MA, 2005.

[46] Sherline Products, http://www.sherline.com, Location - Vista, CA, 2005.

[47] Dassault Systemes, http://ww.3ds.com, 2005.

[48] Sirohi, J., Tishchenko, M., and Chopra, I., "Design and Testing of A Micro-Aerial Vehicle with a Single Rotor and Turning Vanes," 61^{st} *Annual American Helicopter Society Forum*, Grapevine, TX, June 2005.